Minimal models for precipitating turbulent convection

Gerardo Hernandez-Duenas[1]**, Andrew J. Majda**[2]**, Leslie M. Smith**[1,3]
and Samuel N. Stechmann[1,4,†]

[1]Department of Mathematics, University of Wisconsin–Madison, Madison, WI 53706, USA

[2]Department of Mathematics and Center for Atmosphere and Ocean Science, Courant Institute of Mathematical Sciences, New York University, New York, NY 10012-1110, USA

[3]Department of Engineering Physics, University of Wisconsin–Madison, Madison, WI 53706, USA

[4]Department of Atmospheric and Oceanic Sciences, University of Wisconsin–Madison, Madison, WI 53706, USA

Simulations of precipitating convection would typically use a non-Boussinesq dynamical core such as the anelastic equations, and would incorporate water substance in all of its phases: vapour, liquid and ice. Furthermore, the liquid water phase would be separated into cloud water (small droplets suspended in air) and rain water (larger droplets that fall). Depending on environmental conditions, the moist convection may organize itself on multiple length and time scales. Here we investigate the question, what is the minimal representation of water substance and dynamics that still reproduces the basic regimes of turbulent convective organization? The simplified models investigated here use a Boussinesq atmosphere with bulk cloud physics involving equations for water vapour and rain water only. As a first test of the minimal models, we investigate organization or lack thereof on relatively small length scales of approximately 100 km and time scales of a few days. It is demonstrated that the minimal models produce either unorganized ('scattered') or organized convection in appropriate environmental conditions, depending on the environmental wind shear. For the case of organized convection, the models qualitatively capture features of propagating squall lines that are observed in nature and in more comprehensive cloud resolving models, such as tilted rain water profiles, low-altitude cold pools and propagation speed corresponding to the maximum of the horizontally averaged, horizontal velocity.

---

1. Introduction

Convection occurs in the atmosphere in many different contexts, from the planetary boundary layer, to storms that convect through the depth of the troposphere, to the global atmospheric circulation between the equator and the poles. In this paper, the focus is on convection in the tropical troposphere, where deep precipitating clouds can

† Email address for correspondence: stechmann@wisc.edu

be organized into distinctive patterns and sometimes propagate long distances (Houze 2004).

Moist convection in the atmosphere is characterized by the presence of water in its different phases, vapour, liquid and ice, and phase changes between them (Emanuel 1994; Stevens 2005). Dry convection is a useful baseline for comparison (e.g. Chandrasekhar 1961; Deardorff 1965; Asai 1970; Krishnamurti 1970*a*,*b*; Castaing *et al.* 1989). However, beyond the basic physics of dry convection, moist convection involves a multitude of additional physical process: phase changes of water, collisions between cloud droplets and absorption of infrared radiation by water, to name a few. Ultimately, these processes are manifested as the clouds and storm systems seen all around the world.

In the tropical atmosphere, deep moist convection creates a rich variety of cloud structures on many different scales. Individual cloud systems appear on horizontal scales of roughly 100 km and 1 h to 1 day, and they are commonly called 'mesoscale convective systems' (MCSs) (Houze 2004). Several MCSs, in turn, can sometimes interact with propagating waves to form even larger-scale structures such as convectively coupled equatorial waves (Kiladis *et al.* 2009) and the Madden–Julian oscillation (MJO) (Zhang 2005; Lau & Waliser 2011). The MJO is at the largest end of this hierarchy: its oscillation period is 30–60 days and its wavelength is roughly 20 000 km, comparable to the 40 000 km circumference of the Earth at the equator. Also included in this hierarchy are the familiar phenomena of hurricanes and monsoons, which makes it clear that understanding and predicting organized tropical convection has important practical implications.

Despite the importance of organized tropical convection, numerical simulation of it remains a major challenge (Kim *et al.* 2009; Straub, Haertel & Kiladis 2010). It is believed that computational shortcomings are related to gaps in theoretical understanding of the physical processes involved (see Moncrieff *et al.* (2007) and Majda & Stechmann (2011) and references therein). In order to improve theoretical understanding of tropical convection, one can argue that the focus should be on MCSs (Mapes *et al.* 2006), since they are the 'building blocks' of larger-scale structures such as the MJO (Nakazawa 1988; Hendon & Liebmann 1994; Grabowski & Moncrieff 2001). Thus, these MCSs, the small-scale (100 km) moist turbulent coherent structures in the atmosphere, are the focus of the present paper.

Two of the most striking features of MCSs are the different cloud patterns that can arise and their propagation characteristics. For understanding these features, it is common to divide the total system into a large-scale background environment and the smaller-scale convection. From this perspective, observational analyses have shown that it is the vertical shear of the horizontal background wind, $\partial \bar{u}/\partial z$ and $\partial \bar{v}/\partial z$, that controls the organization of the cloud structures: convection is typically unorganized ('scattered') when the wind shear is weak, and it can organize into distinctive patterns in the presence of strong wind shear (Moncrieff & Green 1972; Barnes & Sieckman 1984; Grabowski *et al.* 1998; LeMone, Zipser & Trier 1998). Figure 1 shows a preview of these two cases, scattered and organized convection, from the present paper's model. The case with strong background wind shear, a jet profile here, leads to a common type of MCS called a 'squall line', where the clouds are organized in a line and propagate in the direction perpendicular to the line.

In addition to observational analysis, numerical models called cloud resolving models (CRMs) have also been valuable tools for understanding convective organization. These models are so-named because they use grid spacings of roughly 1 km and hence can, in principle, resolve the dynamics of individual clouds or MCSs;
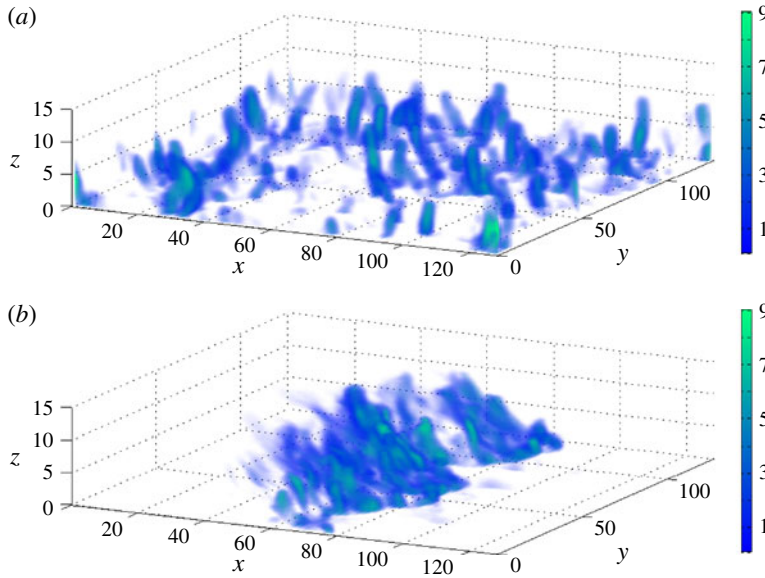
FIGURE 1. (Colour online) Contours of rain water in g kg^{-1} for two cases of numerical solutions using the fast autoconversion and rain evapouration (FARE) minimal model of this paper. The two cases are scattered convection (*a*) and squall lines (*b*).

this is opposed to general circulation models (GCMs) that use grid spacings of roughly 100 km and must parameterize clouds as a subgrid-scale process. While both CRMs and GCMs have deficiencies in representing the largest-scale features of tropical convection (such as the MJO; see Moncrieff *et al.* (2007) and references therein), CRMs can be used to faithfully simulate MCSs. In particular, on smaller domains with horizontal scales of 100–1000 km, CRMs are able to reproduce different cloud regimes, e.g. scattered convection versus a squall line, in response to different background wind shear (Grabowski *et al.* 1998), and they can provide further details that are often unavailable from observational data. It has also been shown that some basic regimes of organization can be reproduced in a two-dimensional (2D) (x, z) set-up, where it is assumed that structures are uniform in one of the horizontal directions (*y*) (Lafore & Moncrieff 1989; Grabowski, Wu & Moncrieff 1996; Xu & Randall 1996; Wu, Grabowski & Moncrieff 1998; Lucas, Zipser & Ferrier 2000; Liu & Moncrieff 2001).

For better or for worse, CRMs are comprehensive in the sense that they attempt to include all relevant physical processes (as discussed further below). While this is a proper approach when trying to make weather predictions or detailed comparisons with observations, it may be obscuring some fundamental aspects of precipitating convection, as it is not clear which processes are 'essential', in some sense, and which are not. For example, are there fundamental features of precipitating convection that are more-or-less insensitive to many model details? In particular, is there a theoretical explanation for the preferred cloud patterns (or lack thereof) that appear due to a given background wind shear, $\partial \bar{u}/\partial z$ and $\partial \bar{v}/\partial z$ (Grabowski *et al.* 1998; LeMone *et al.* 1998)? Questions such as these have long been investigated by the atmospheric science community (see reviews by Lilly (1979), Houze (2004) and Moncrieff (2010) and further discussion at the end of this section). These are difficult questions to answer if

all of the comprehensive physics of CRMs is essential, but it may be more tractable if a minimal number of essential processes can be identified. Here, a further step in this direction is demonstrated: a much simpler model than typical CRMs can reproduce the basic regimes of precipitating turbulent convection.

In other words, in the present paper, one of the main goals is to identify and investigate a minimal model that can capture the broad features of precipitating turbulent convection. Specifically, the minimal model should capture the basic regimes of convective organization, scattered convection versus a squall line, in response to different background wind shears, and the basic realistic features of the squall line should be captured: propagation direction, propagation speed, circulation and tilted cloud structure. It is shown here that these features can be captured by a set of equations that is simpler than those used by comprehensive CRMs; it is, in fact, quite similar to those typically used for non-precipitating moist convection (Kuo 1961; Bretherton 1987; Cuijpers & Duynkerke 1993; Grabowski & Clark 1993; Spyksma, Bartello & Yau 2006; Stevens 2007; Spyksma & Bartello 2008; Pauluis & Schumacher 2010, 2011). Precipitation-cooled downdrafts are a main feature distinguishing deep convection (vertical scales approximately the height of the troposphere, 10 km) from non-precipitating shallow convection (vertical scales of approximately 1 km). The presence of rain water and a rainfall velocity in our models is thus a key difference from similar models used to understand aspects of shallow convection and/or focusing specifically on small-scale moist turbulence. For shallow convection, simplified moist models are concerned mainly with water vapour and cloud water (small liquid droplets suspended in air).

The minimal models include simplifications in two main aspects: thermodynamics and cloud microphysics. As discussed in more detail below, the simplified thermodynamics will be based on the following design principle: the conservation laws for momentum, energy, moist entropy and total water should all be retained, but they should have the simplest non-trivial form possible. Furthermore, the cloud microphysics will not only neglect ice, but it will also assume that cloud droplets, once formed, grow rapidly to the size of rain drops, which fall relative to the air in which they reside. In other words, this 'autoconversion process' is assumed to be fast compared with the dynamical scales of interest. Two-dimensional simulations of a similar model were investigated by Seitter & Kuo (1983), and instabilities of a linear model with fast autoconversion (FA) were investigated by Emanuel (1986). Fast autoconversion was also used by Majda, Xing & Mohammadian (2010) with a weak-temperature-gradient approximation for studying the hurricane embryo. Relaxing the weak-temperature-gradient approximation and allowing inertia-gravity waves, Sukhatme, Majda & Smith (2012) studied 2D precipitating stratified turbulence with fast autoconversion, and Deng, Smith & Majda (2012) used a three-dimensional (3D) Boussinesq model with fast autoconversion to investigate the competing effects of moisture and low-altitude vertical shear for cyclogenesis. Here the simplified microphysics is put to a further test, where it is used with a dynamical core that includes internal gravity wave dynamics and where the ultimate goal is to achieve a full range of convective organization.

Even more simplified than the models considered here, there is a class of archetypal models which is 2D and steady in the reference frame moving with the squall line (Moncrieff & Green 1972; Moncrieff & Miller 1976; Moncrieff 1981, 1992). Solutions to the 2D steady models provide a theoretical basis for canonical circulation patterns and momentum transport associated with different inflow–outflow boundary conditions and background shear profiles. These solutions can be combined to capture elements

of more complicated patterns associated with observed and computed regimes of organized convection, including squall lines (Moncrieff 1992, 2010). Here, in contrast, we investigate models which are 3D and unsteady, but which nevertheless reflect a minimalist approach to incorporate phase changes of water and precipitation within the context of a 3D dynamical core. They allow for turbulence, even though our modest resolutions (1 km in the horizontal directions) do not capture turbulence at the smallest atmospheric scales, as is also the case in typical contemporary CRM simulations.

The paper is organized as follows. In § 2, the minimal models are introduced and compared with the equations of a comprehensive CRM. In §§ 3 and 4, 3D numerical simulations of the minimal models are presented for the basic regimes of convective organization (scattered convection and a squall line). In §§ 5 and 6 sensitivity studies are used to explore the robustness of the results. Finally, in § 7, the main conclusions are summarized.

2. Model descriptions

In this section, three models are described. First, a representative comprehensive CRM is presented as a basis for comparison. Then two simplified models are presented and used as the main models of the present paper.

2.1. *A representative comprehensive model*

An atmospheric CRM could be based on the anelastic equations for moist air with at least three phases of water: cloud water q_c, rain water q_r and water vapour q_v. Each of the quantities q_v, q_c, q_r is a mixing ratio measured in kilograms of water per kilogram of dry air. More comprehensive models would include other phases of water such as ice. Derivations of the anelastic equations can be found in, e.g. Ogura & Phillips (1962), Lipps & Hemler (1982), Bannon (1996) and Vallis (2006). Here we use the symbols $\tilde{\rho}(z), \tilde{p}(z), \tilde{T}(z), \tilde{\theta}(z)$ to denote the anelastic background states of density, pressure, temperature and potential temperature, respectively. The anelastic approximation assumes that $\tilde{\rho}(z)$ and $\tilde{p}(z)$ are hydrostatically balanced and that all deviations from the background state variables are small. The depth of the fluid motions is comparable to the density scale height $H_\rho = -\tilde{\rho}\,(\mathrm{d}\tilde{\rho}/\mathrm{d}z)^{-1}$; time scales are comparable to the buoyancy time scale and much longer than the time scale associated with acoustic waves. Including cloud physics, the anelastic equations may be written as

$$\frac{\mathrm{D}\boldsymbol{u}}{\mathrm{D}t} = -\boldsymbol{\nabla}\left(\frac{p'}{\tilde{\rho}(z)}\right) + \boldsymbol{k}g\left(\frac{\theta - \tilde{\theta}(z)}{\tilde{\theta}(z)} + \varepsilon_o(q_v - \tilde{q}_v(z)) - q_c - q_r\right) \qquad (2.1)$$

$$\boldsymbol{\nabla}\cdot(\tilde{\rho}(z)\boldsymbol{u}) = 0 \qquad (2.2)$$

$$\frac{\mathrm{D}\theta}{\mathrm{D}t} = \frac{L\tilde{\theta}(z)}{c_p\tilde{T}(z)}(C_d - E_r) \qquad (2.3)$$

$$\frac{\mathrm{D}q_v}{\mathrm{D}t} = -C_d + E_r \qquad (2.4)$$

$$\frac{\mathrm{D}q_c}{\mathrm{D}t} = C_d - A_r - C_r \qquad (2.5)$$

$$\frac{\mathrm{D}q_r}{\mathrm{D}t} - \frac{1}{\tilde{\rho}(z)}\frac{\partial}{\partial z}(\tilde{\rho}(z)V_T q_r) = A_r + C_r - E_r \qquad (2.6)$$
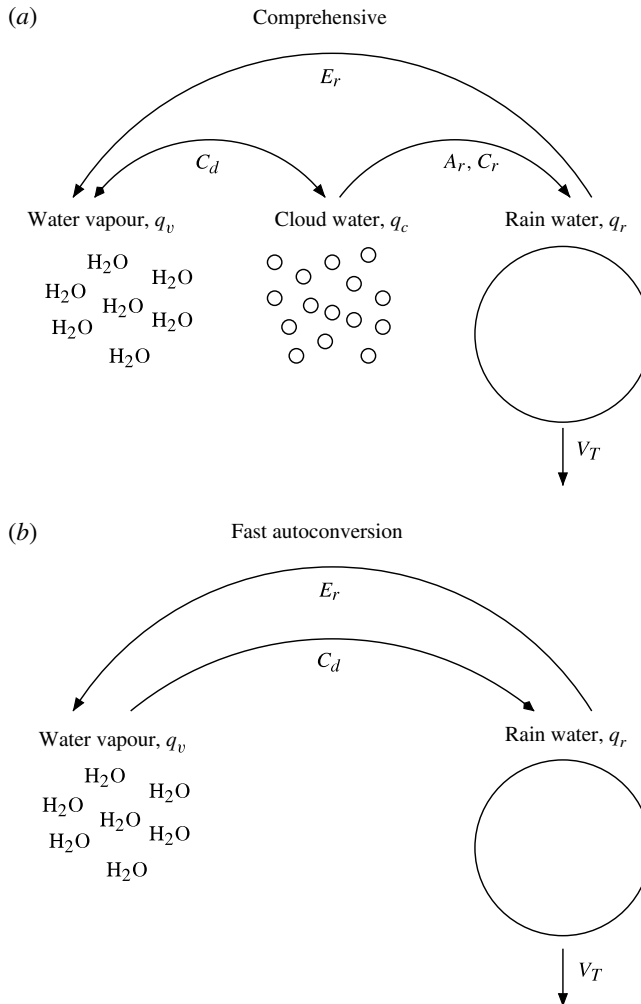
(*a*) Comprehensive

E_r

C_d A_r, C_r

Water vapour, q_v Cloud water, q_c Rain water, q_r

H_2O H_2O
H_2O H_2O
H_2O H_2O
H_2O

V_T

(*b*) Fast autoconversion

E_r

C_d

Water vapour, q_v Rain water, q_r

H_2O H_2O
H_2O H_2O
H_2O H_2O
H_2O

V_T

FIGURE 2. Schematic diagrams of cloud physics in numerical models. (*a*) A representative form of cloud physics in a comprehensive CRM without ice processes. Three categories of water are used. See (2.1)–(2.6). (*b*) A simplified form of fast autoconversion cloud physics where autoconversion (A_r) of cloud water q_c to rain water q_r is assumed to occur rapidly. Only two categories of water are used. See (2.9)–(2.13) and (2.35)–(2.38).

where $\boldsymbol{u}(\boldsymbol{x}, t)$ is the velocity vector with components (u, v, w), $\boldsymbol{k}$ is the direction of gravity, and the material derivative is defined as $D/Dt = \partial/\partial t + \boldsymbol{u} \cdot \nabla$. The total thermodynamic variables $\rho(\boldsymbol{x}, t)$, $p(\boldsymbol{x}, t)$, $\theta(\boldsymbol{x}, t)$ and $T(\boldsymbol{x}, t)$ are all decomposed into the anelastic background and deviation, e.g. $\rho(\boldsymbol{x}, t) = \tilde{\rho}(z) + \rho'(\boldsymbol{x}, t)$ with $|\rho'| \ll |\tilde{\rho}|$, etc. Similarly the total water vapour $q_v(\boldsymbol{x}, t) = \tilde{q}_v(z) + q_v'(\boldsymbol{x}, t)$. The relation between temperature and potential temperature is

$$T = \left(\frac{p}{p_o}\right)^{R_d/c_p} \theta, \qquad (2.7)$$

where $p_o \approx 10^5$ kg m^{-1} s^{-2} is the pressure reference at the surface. The source terms on the right-hand-side of (2.3)-(2.6) are condensation C_d of water vapour to form cloud water, evapouration E_r of rain water to form water vapour, auto-conversion A_r of cloud water to form rain water, and collection C_r of cloud water to form rain water. Each source term requires modelling of either the detailed microphysics involving individual droplets, or the bulk physics with closures involving the mixing ratios q_v, q_c, q_r (Kessler 1969; Houze 1993; Emanuel 1994; Grabowski & Smolarkiewicz 1996). The condensation C_d and evapouration E_r depend on a saturation profile $q_{vs}(p, T)$ determined using the Clausius–Clapeyron relation (Rogers & Yau 1989; Houze 1993; Emanuel 1994; Pruppacher & Klett 1997). One must also specify the rain velocity V_T, which in principle depends on droplet size. The remaining quantities appearing in the system (2.1)–(2.6) are the specific heat at constant pressure c_p, the latent heat factor L and the ratio of gas constants $R_v/R_d = \varepsilon_o + 1$ for water vapour (R_v) and dry air (R_d). Typical values are $c_p \approx 10^3$ J kg^{-1} K^{-1}, $L \approx 2.5 \times 10^6$ J kg^{-1}, $R_d \approx 287$ J kg^{-1} K^{-1}, $R_v \approx 462$ J kg^{-1} K^{-1} and $\varepsilon_o \approx 0.6$.

2.2. *An approximation for the saturation water vapour profile*

As mentioned above, the cloud physics source terms depend on the saturation water vapour $q_{vs}(p, T)$, which is a function of temperature and pressure only (Rogers & Yau 1989). This function $q_{vs}(p, T)$ is the maximum amount of water vapour that air can hold: if q_v reaches the value of q_{vs}, then some water vapour will condense into liquid water q_c in order to maintain $q_v \leqslant q_{vs}$. In a comprehensive treatment of moist thermodynamics, which would be required for a CRM such as (2.1)–(2.6), the form of the function $q_{vs}(p, T)$ is determined by the Clausius–Clapeyron relation (Rogers & Yau 1989). Here, for the simplified models that are presented next, $q_{vs}(p, T)$ is approximated as $q_{vs}(z)$, a function of height only.

To arrive at the approximation $q_{vs} \approx q_{vs}(z)$, recall the anelastic approximation assumes that $p(\boldsymbol{x}, t) \approx \tilde{p}(z)$ and $T(\boldsymbol{x}, t) \approx \tilde{T}(z)$. Hence

$$q_{vs}(p, T) \approx q_{vs}(\tilde{p}(z), \tilde{T}(z)) \equiv q_{vs}(z). \tag{2.8}$$

A systematic asymptotic analysis of (2.8) and higher-order terms is given by Klein & Majda (2006). The form of $q_{vs}(z)$ used here is shown in figure 3 and described in more detail in appendix A.

2.3. *A Boussinesq model with fast autoconversion (FA)*

One can see that there are many functions to be specified when implementing the anelastic model (2.1)–(2.6): $\tilde{\rho}(z), \tilde{p}(z), \tilde{T}(z), \tilde{\theta}(z), \tilde{q}_v(z), C_d, E_r, A_r, C_r, V_T$. To target particular atmospheric conditions, one may choose the background thermodynamic state from observations. However, here we aim to reduce the number of externally defined functions and parameters while still retaining essential features of precipitating, organized convection. It is natural (although unjustified for deep convection) to invoke the Boussinesq approximation, which requires that the depth of fluid motions be small compared with the density scale height $H_\rho = -\tilde{\rho}\,(\mathrm{d}\tilde{\rho}/\mathrm{d}z)^{-1}$ (Spiegel & Veronis 1960; Vallis 2006). Then the undifferentiated base state density, pressure, temperature and potential temperature in (2.1)–(2.6) may be replaced by constant values, where each has been decomposed as e.g. $\tilde{\theta}(z) = \theta_o + \tilde{\theta}'(z)$. Then we need only specify $\mathrm{d}\tilde{\theta}(z)/\mathrm{d}z$, $\mathrm{d}\tilde{q}_v(z)/\mathrm{d}z$ as well as C_d, E_r, A_r, C_r, V_T.

Next we consider the limit of fast autoconversion A_r such that water vapour is converted directly into rain water (Majda *et al.* 2010; Deng *et al.* 2012). In this
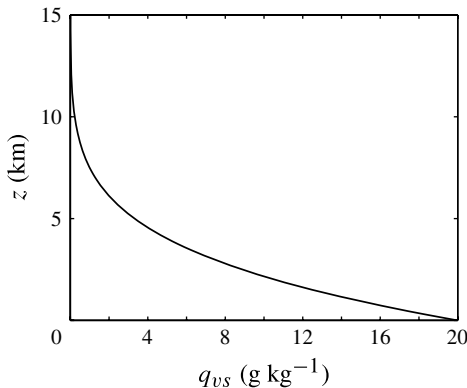
FIGURE 3. Saturation moisture profile $q_{vs}(z)$ computed using relations (A 7)–(A 8) and $q_{vs,o} = 20$ g kg^{-1}.

scenario, the excess water vapour above saturation can be interpreted as cloud water, and there is no need to solve explicitly for cloud water q_c, or to include expressions for autoconversion A_r and collection C_r. This simplification means that we must use bulk models for condensation C_d and evaporation E_r (as opposed to detailed cloud microphysics). Finally, assuming a constant rainfall velocity V_T and a linear background potential temperature $\theta = \theta_o + Bz + \theta'(\boldsymbol{x}, t)$, $\theta_o = T_o \approx 300$ K, $B \approx 3 \times 10^{-3}$ K m^{-1}, we arrive at a Boussinesq model with fast autoconversion and denoted FA:

$$\frac{D\boldsymbol{u}}{Dt} = -\nabla \phi + \boldsymbol{k}\, g \left(\frac{\theta - \tilde{\theta}(z)}{\theta_o} + \varepsilon_o(q_v - \tilde{q}_v(z)) - q_r \right) \tag{2.9}$$

$$\nabla \cdot \boldsymbol{u} = 0 \tag{2.10}$$

$$\frac{D\theta}{Dt} = \frac{L}{c_p}(C_d - E_r) \tag{2.11}$$

$$\frac{Dq_v}{Dt} = -C_d + E_r \tag{2.12}$$

$$\frac{Dq_r}{Dt} - V_T \frac{\partial q_r}{\partial z} = C_d - E_r \tag{2.13}$$

where $\phi = p'/\rho_o$. So far, one could argue that the only adjustable parameters/functions in the FA model are the expressions for condensation C_d, evapouration E_r, background vapour profile $\tilde{q}_v(z)$, water vapour at saturation $q_{vs}(z)$ and rainfall velocity V_T, since the values of c_p, L, T_o, θ_o and B are well established from observations.

Following Majda *et al.* (2010) and Deng *et al.* (2012), we adopt the closures

$$C_d = \tau_c^{-1} (q_v - q_{vs}(z))^+, \quad E_r = \tau_e^{-1} q_*^{-1} (q_{vs}(z) - q_v)^+ q_r \tag{2.14}$$

where the notation $(\ )^+$ denotes the positive part and $q_{vs}(z)$ is shown in figure 3 and given in the appendix in (A 7)–(A 8). Equations (2.14) imply that condensation occurs if the water vapour exceeds the saturation value, and similarly evapouration occurs if the fluid is undersaturated and if rain is present. In our simulations we use $q_* = 0.01$ kg kg^{-1}. The time scales τ_c and τ_e are analogous to chemical reaction rates

and the related Damköhler numbers in turbulent combustion (Majda & Souganidis 2000; Peters 2000).

2.4. *A Boussinesq model with fast autoconversion and rain evapouration*

Condensation occurs on a time scale of several seconds, whereas the characteristic time for autoconversion or rain evapouration is many minutes (Rogers & Yau 1989; Houze 1993; Morrison & Grabowski 2008). Thus, it is sensible to formulate a model with fast condensation $\tau_c \to 0$ and fast rain evapouration $\tau_e \to 0$ in addition to fast autoconversion. This model is referred to here as the fast autoconversion and rain evapouration (FARE) model. In such a model there is no possibility for supersaturation, i.e. for $q_v - q_{vs} > 0$, because q_v is instantaneously relaxed back toward $q_{vs}(z)$. Furthermore, rain water q_r cannot exist in unsaturated air because it is instantaneously evapourated until q_v is brought up to saturation q_{vs}. In summary, in the limit $\tau_c, \tau_e \to 0$, the source terms C_d and E_r maintain the following constraints and are actually defined so as to maintain these constraints:

$$\text{either} \quad q_v < q_{vs}, \quad q_r = 0 \quad \text{(unsaturated)} \tag{2.15}$$

$$\text{or} \quad q_v = q_{vs}, \quad q_r \geqslant 0 \quad \text{(saturated)}. \tag{2.16}$$

This formulation is commonly used in CRMs except with q_c rather than q_r (e.g. Grabowski & Smolarkiewicz 1996). Owing to these constraints, the two variables q_v and q_r are now more than necessary to determine the partitioning of water substance in the system. This is because the single variable $q_t = q_v + q_r$, called the total water mixing ratio, is sufficient to determine both q_v and q_r using the constraints (2.15)–(2.16):

$$q_v = q_t, \quad q_r = 0 \quad \text{if } q_t < q_{vs} \quad \text{(unsaturated)} \tag{2.17}$$

$$q_v = q_{vs}, \quad q_r = q_t - q_{vs} \quad \text{if } q_t \geqslant q_{vs} \quad \text{(saturated)}. \tag{2.18}$$

Consequently, only two thermodynamic variables are needed now instead of the three variables θ, q_v, q_r.

For particular choices of thermodynamic variables in this limit of $\tau_c, \tau_e \to 0$, it is convenient to choose variables that are conserved in the sense that the source terms C_d and E_r do not change their values. From (2.11)–(2.13), one can see three different conserved variables,

$$\theta_e = \theta + \frac{L}{c_p} q_v \tag{2.19}$$

$$\theta_r = \theta - \frac{L}{c_p} q_r \tag{2.20}$$

$$q_t = q_v + q_r, \tag{2.21}$$

which satisfy the equations

$$\frac{D\theta_e}{Dt} = 0 \tag{2.22}$$

$$\frac{D\theta_r}{Dt} = -\frac{L}{c_p} V_T \frac{\partial q_r}{\partial z} \tag{2.23}$$

$$\frac{Dq_t}{Dt} = V_T \frac{\partial q_r}{\partial z}. \tag{2.24}$$

These variables are called the equivalent potential temperature, θ_e, the rain water potential temperature, θ_r, and the total water mixing ratio, q_t, and they are linearized versions of analogous variables used in comprehensive treatments of moist thermodynamics (Rogers & Yau 1989; Emanuel 1994; Stevens 2005). Note that we have 'minimized' even more from the FA model in the sense that we do not need to specify closures for condensation C_d and evapouration E_r.

The FARE model consists of (2.9) and (2.10) together with two of (2.22)–(2.24). A common choice is to use θ_r and q_t (Stevens 2005, 2007) and this choice is used in the present paper. For the buoyancy term in (2.9), one must compute θ, q_v and q_r from θ_r and q_t; this is done using (2.17)–(2.21):

$$\theta = \theta_r + \frac{L}{c_p}q_t - \frac{L}{c_p}\min(q_t, q_{vs}(z)) \tag{2.25}$$

$$q_v = \min(q_t, q_{vs}(z)) \tag{2.26}$$

$$q_r = \max(q_t - q_{vs}(z), 0). \tag{2.27}$$

In other words, while the buoyancy is a linear function of θ, q_v and q_r, it is a piecewise linear function of θ_r and q_t. Specifically, $b = b(\theta_r, q_t, z)$ is given by

$$b = g \begin{cases} \dfrac{\theta_r - \tilde{\theta}(z)}{\theta_o} + \varepsilon_o(q_t - \tilde{q}_v(z)) & \text{if } q_t < q_{vs} \\[2ex] \dfrac{\theta_r - \tilde{\theta}(z)}{\theta_o} + \left(\dfrac{L}{c_p\theta_o} - 1\right)(q_t - q_{vs}(z)) + \varepsilon_o(q_{vs}(z) - \tilde{q}_v(z)) & \text{if } q_t \geqslant q_{vs}. \end{cases} \tag{2.28}$$

FARE is similar to models used for non-precipitating shallow convection in the atmosphere (Cuijpers & Duynkerke 1993; Stevens 2005, 2007) or moist Rayleigh–Bénard convection (Schumacher & Pauluis 2010; Pauluis & Schumacher 2011), which use nearly the same equations except with $V_T = 0$. Here we will show that, despite their relative simplicity, the FARE equations are sufficient to capture the basic features of precipitating organized convection.

In summary, one could take two different viewpoints of the FARE model. On the one hand, it can be obtained from a comprehensive CRM by employing some simplifications: the limit of fast cloud physics time scales (for autoconversion, condensation and rain evapouration), and assuming a Boussinesq rather than anelastic atmosphere. From a mathematical point of view, these simplifications follow a design principle of obtaining the simplest set of equations that retain conservation principles for θ_e, θ_r and q_t. On the other hand, the FARE model can be obtained from a non-precipitating convection model (e.g. Cuijpers & Duynkerke 1993; Stevens 2007) by allowing the condensed water to fall at speed V_T. From a physical point of view, this is similar to assuming an atmosphere where all liquid droplets are large enough to fall relative to the surrounding air.

2.5. *Summary of the FA and FARE models*

For clarity, we write the final form of the FA and FARE models.

The final FA model is

$$\frac{D\boldsymbol{u}}{Dt} = -\boldsymbol{\nabla}\phi + \boldsymbol{k}\,g\left(\frac{\theta - \tilde{\theta}(z)}{\theta_o} + \varepsilon_o(q_v - \tilde{q}_v(z)) - q_r\right) \tag{2.29}$$

$$\boldsymbol{\nabla} \cdot \boldsymbol{u} = 0 \tag{2.30}$$

$$\frac{D\theta}{Dt} = \frac{L}{c_p}(C_d - E_r) \tag{2.31}$$

$$\frac{Dq_v}{Dt} = -C_d + E_r \tag{2.32}$$

$$\frac{Dq_r}{Dt} - V_T \frac{\partial q_r}{\partial z} = C_d - E_r \tag{2.33}$$

$$C_d = \tau^{-1} (q_v - q_{vs}(z))^+, \quad E_r = \tau^{-1} q_*^{-1} (q_{vs}(z) - q_v)^+ q_r \tag{2.34}$$

and the final FARE model is

$$\frac{D\boldsymbol{u}}{Dt} = -\nabla\phi + \boldsymbol{k}\, b(\theta_r, q_t, z) \tag{2.35}$$

$$\nabla \cdot \boldsymbol{u} = 0 \tag{2.36}$$

$$\frac{D\theta_r}{Dt} + \frac{L}{c_p} V_T \frac{\partial q_r}{\partial z} = 0 \tag{2.37}$$

$$\frac{Dq_t}{Dt} - V_T \frac{\partial q_r}{\partial z} = 0 \tag{2.38}$$

where the form of the buoyancy $b(\theta_r, q_t, z)$ is given in (2.28). In both FA and FARE, we use standard values of thermodynamic constants $c_p \approx 10^3$ J kg^{-1} K^{-1}, $L \approx 2.5 \times 10^6$ J kg^{-1}, $\theta_o \approx 300$ K, $T_o \approx 300$ K, $p_o \approx 10^5$ kg m^{-1} s^{-2}, $R_d \approx 287$ J kg^{-1} K^{-1}, $R_v \approx 462$ J kg^{-1} K^{-1}, $\varepsilon_o \approx 0.6$, $q_{vs,o} = (R_d/R_v)(e_{s,o}/p_o) = 2 \times 10^{-2}$ kg kg^{-1} and $e_{s,o} \approx 3500$ kg m^{-1} s^{-2}. The rainfall velocity is fixed at $V_T = 5$ m s^{-1} and the background moisture profile $\tilde{q}_v(z)$ will be slightly undersaturated at all altitudes. The background potential temperature gradient is $B \approx 3 \times 10^{-3}$ K m^{-1}.

2.6. *Conservation principles*

As mentioned above, both the FA and FARE models conserve the equivalent potential temperature θ_e, the rain-water potential temperature θ_r and total water q_t. It seems likely that these conservation relations are an underlying reason why the FA and FARE models are able to capture broad features of organized convection shown below.

In addition, the FARE model has an energy consistency equation given by

$$\frac{\partial}{\partial t}\left(\frac{\boldsymbol{u} \cdot \boldsymbol{u}}{2} + \Pi\right) + \nabla \cdot \left[\boldsymbol{u}\left(\frac{\boldsymbol{u} \cdot \boldsymbol{u}}{2} + \Pi + \phi\right)\right] - \frac{\partial}{\partial z}[V_T g(z - a)q_r] = -V_T g q_r. \tag{2.39}$$

In (2.39), the potential energy Π is given by Vallis (2006) and Pauluis (2008)

$$\Pi(\theta_r, q_t, z) = -\int_a^z b(\theta_r, q_t, z')dz' \tag{2.40}$$

where the integral is taken with θ_r and q_t held fixed, and a is an arbitrary reference height. The derivation of (2.39) is given in appendix B. Note the two terms in (2.39) with a factor of V_T: a rain flux term and a sign-definite energy sink. The energy sink term is consistent with an interpretation of the $-gq_r$ term of the buoyancy (Houze 1993; Pauluis, Balaji & Held 2000; Pauluis & Dias 2012): if liquid droplets fall (i.e. $V_T \neq 0$) relative to the surrounding air, then they should exert a frictional drag force $-gq_r$ on the surrounding air. The FARE energy equation (2.39) is an interesting additional feature of the model, but we leave an in-depth investigation of the energetics for future work.

2.7. *Numerical scheme and simulation details*

The 3D simulations in §§ 3 and 4 are computed in a numerical domain (x, y, z) of size 128 km $\times$ 128 km $\times$ 15 km, with periodic boundary conditions in the horizontal directions and a combination of Dirichlet/Neumann boundary conditions on vertical boundaries. The numerical scheme is based on a pseudo-spectral decomposition in the horizontal directions, and second-order centred differences on a staggered grid in the vertical direction. In order to be comparable to studies of organized convection with comprehensive CRMs (Grabowski *et al.* 1996, 1998), we use 1 km horizontal grid spacing and 0.15 km vertical grid spacing, i.e. $\Delta x = \Delta y = 1$ km and $\Delta z = 0.15$ km). For our 3D domain, this choice leads to 128 Fourier modes in each horizontal direction and 100 levels in the vertical direction. The, 2D sensitivity studies in §§ 5 and 6 use a numerical domain of size 256 km $\times$ 15 km, again with $\Delta x = 1$ km and $\Delta z = 0.15$ km, and thus 256 Fourier modes in the horizontal direction and 100 levels in the vertical direction.

For no flow through the top and bottom of the domain, the vertical velocity w satisfies the zero Dirichlet conditions

$$w|_{z=0,H} = 0, \tag{2.41}$$

where $H = 15$ km. In the spirit of constructing a minimal model, we do not attempt to model or resolve the atmospheric boundary layer. The horizontal velocity satisfies zero Neumann boundary condition at the top and zero Dirichlet boundary condition at the bottom such that

$$\left.\frac{\partial \boldsymbol{u}_h}{\partial z}\right|_{z=H} = 0, \quad \boldsymbol{u}_h|_{z=0} = 0. \tag{2.42}$$

For all other variables, zero Neumann boundary conditions are applied to perturbations f from the background states such that

$$\left.\frac{\partial f}{\partial z}\right|_{z=0,H} = 0 \tag{2.43}$$

for $f = \theta', q_v', q_r, \theta_r', \theta_e', q_t'$.

The FA and FARE systems are integrated in time using a third-order Runge–Kutta scheme. The time step is usually $\Delta t \approx 2.2$ s, and satisfies the Courant–Friedrichs–Lewy (CFL) condition, a condition that samples the highest-frequency inertia-gravity wave with at least 10 steps per period, and a condition that restricts the time step to be less than one half of the relaxation time scales used in the squall line simulations. We use the same dissipation in each of the equations, with the goal of reducing as much as possible the effects of dissipation on the grid box of 1 km $\times$ 1 km $\times$ 0.15 km. Since the molecular viscosity does not act on these scales, the dissipation operators and coefficients are artificial and can be viewed as a device to dissipate a sufficient amount of energy; here we do not attempt to provide a more sophisticated subgrid model. For simplicity of implementation within our numerical scheme, we choose a normal viscosity operator $\mu_1 \partial^2 f / \partial^2 z$ in the vertical direction (with finite differences), and a fourth-order hyperviscosity operator $-\mu_2 \nabla_h^4 f$ (with Fourier decomposition), where $f = \boldsymbol{u}_h, w, \theta, q_v, q_r, \theta_r, q_t$. The coefficients μ_1 and μ_2 were chosen by experimentation to be as small as possible while still providing an adequate range of supergrid scales with rapid decay of energy in the tail of the vertically averaged kinetic energy spectrum.
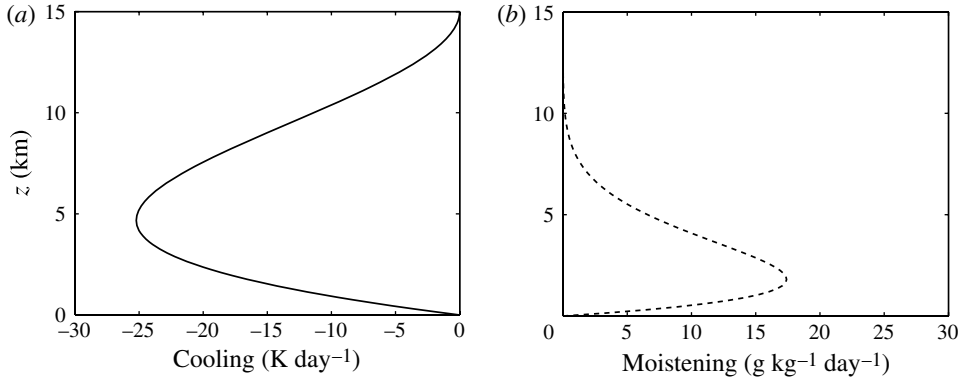
FIGURE 4. Cooling (*a*) and moistening (*b*) rate profiles used as a large-scale forcing in the 3D simulations.

The rainfall velocity V_T of a droplet depends on several conditions such as the drop size, temperature and pressure. Obtained at sea level conditions, a table of typical rainfall velocities as a function of the diameter of the droplets is shown in Rogers & Yau (1989). The velocity changes from approximately 0.3 to 10 m s^{-1} for droplets of size 0.1–6 mm, respectively. A constant rainfall velocity of $V_T = 5.5$ m s^{-1} in the middle of the range has been adopted for all simulations aimed at keeping the model minimal. An exception occurs in § 6.1, where a sensitivity study to different values of V_T is presented.

A moisture source is needed to sustain precipitating convection and replenish the water lost through precipitation. A natural moisture source is the flux of moisture from the surface, which is transported to higher altitudes through turbulence in the moist atmospheric boundary layer (Stevens 2005, 2007). These processes mostly operate on subgrid scales in the current set-up and, for the sake of simplicity, no attempt has been made to parameterize these effects here. Instead, another moisture source that is commonly used is a 'large-scale forcing' that is independent of x and y (e.g. Grabowski *et al.* 1996; Jung & Arakawa 2005). This large-scale forcing is meant to represent the effects of larger-scale phenomena, such as moisture convergence due to larger-scale waves, on the simulated domain. While this large-scale forcing is somewhat artificial, it is commonly used in conjunction with periodic boundary conditions and when computational expense demands a limited domain size. Figure 4 shows the vertical profiles for the moistening/cooling rates used in the 3D simulations here, with maximum moistening rate roughly 17 g kg^{-1} day^{-1} and maximum cooling rate 25 K day^{-1}. The rates have been reduced by a factor of two in the 2D studies, in accordance with the twice-larger horizontal domain length in those cases, and § 6.4 shows that the rates may be further reduced (or eliminated) in even larger horizontal domains.

The initial conditions for all variables in all runs are the same, with the exception of the zonal velocity which is zero for scattered convection and has a jet profile for squall line runs. The relaxation of the horizontal velocities to the appropriate background winds is described in § 3. The initial water vapour profile is close to saturation, and given by (A 8) in the appendix with $q_{v,0} = 18$ g kg^{-1} instead of $q_{vs,0} = 20$ g kg^{-1}. Both the initial water vapour and water vapour at saturation are plotted in figure 5. The rain water q_r and the vertical velocity w are initially zero. The potential temperature is
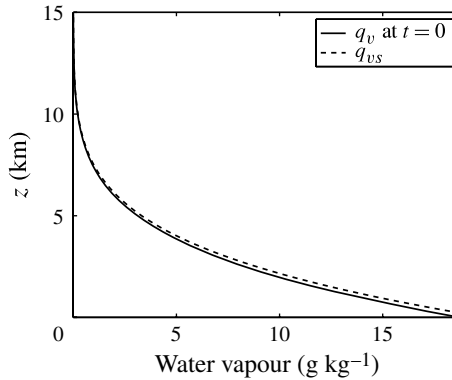
FIGURE 5. The water vapour at $t = 0$ (solid line) is initially set close to saturation (dashed line).

a random perturbation chosen from a uniform distribution in $[-0.1, 0.1]$ at all points (x, y, z) with $0 \leqslant z \leqslant 2$ km. In the squall line simulation, organization of the clouds occurs after a spin-up time of several hours.

The following notation will be needed in the description of the numerical results and figure captions. For any variable $f(x, y, z, t)$, the horizontal and vertical averages $\bar{f}(z, t)$ and $\langle f \rangle(x, y, t)$ are defined respectively as

$$\bar{f}(z, t) := \frac{1}{A_h} \int f(x, y, z, t) \, dx \, dy \tag{2.44}$$

and

$$\langle f \rangle(x, y, t) := \frac{1}{H} \int_0^H f(x, y, z, t) \, dz. \tag{2.45}$$

Here A_h is the horizontal area and $H = 15$ km is the vertical extent of the numerical domain. In addition, the fluctuation of f from its horizontal mean is defined as

$$f''(x, y, z, t) := f(x, y, z, t) - \bar{f}(z). \tag{2.46}$$

3. Numerical results for the 3D FARE model

This section is devoted to the numerical results of the FARE model. As explained in the introduction, the vertical shear of the horizontally averaged, horizontal velocity $\partial \bar{\boldsymbol{u}}_h(z)/\partial z$ controls the organization of the cloud structures. Scattered convection is observed when the background wind shear is weak (§ 3.1), while a strong-enough background jet profile is favourable for organization of the convection into a squall line (§ 3.2). Note that, while 'cloud water' is not explicit in our models by the assumption of fast autoconversion, we will nevertheless use the terminology 'cloud' for saturated regions with $q_r > 0$, which represent suspensions of sedimenting water drops.

3.1. *Scattered convection*

In the simulations designed to represent scattered convection, the horizontal velocities are initially set to zero. Then the horizontally averaged, horizontal velocity $\bar{\boldsymbol{u}}_h(z)$ is relaxed towards zero during the simulation by adding a source term to the right-hand
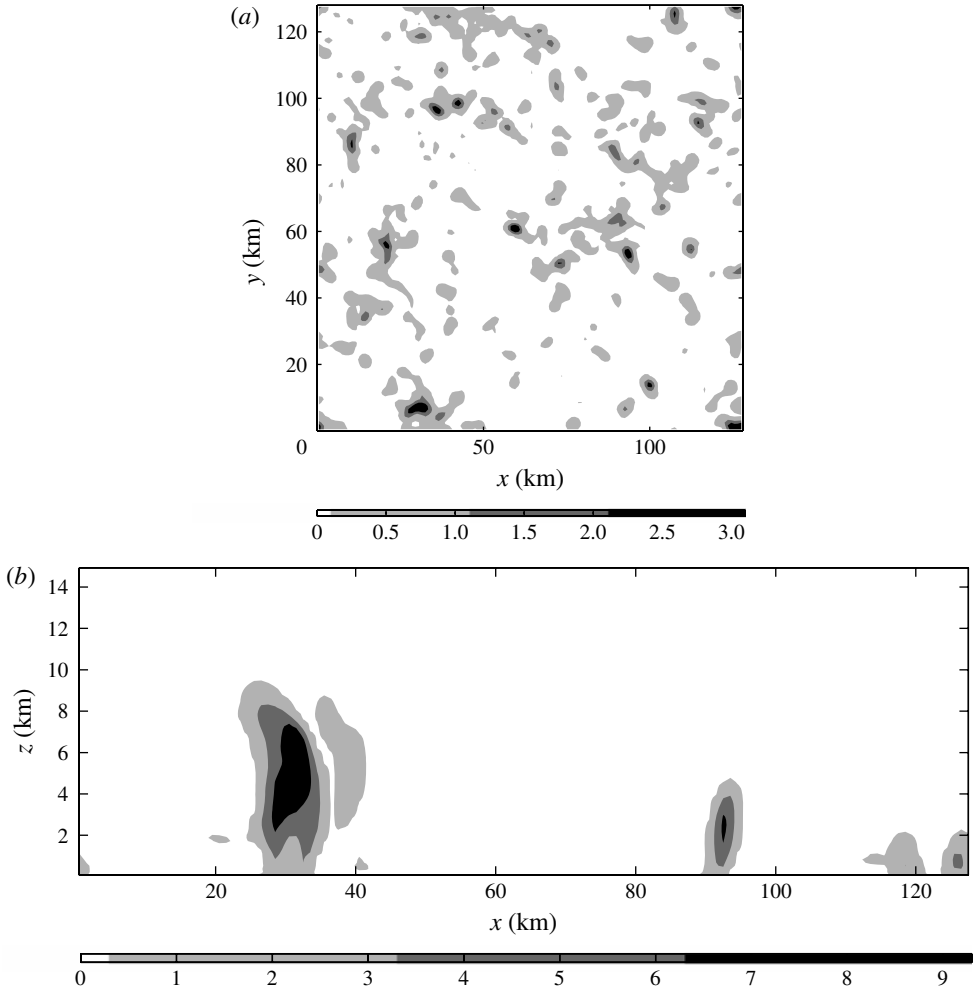
FIGURE 6. Scattered convection in a 3D simulation of the FARE model at time $t = 4.8$ h. (*a*) Contours of vertically averaged rain water $\langle q_r \rangle(x, y)$. (*b*) Contours of rain water q_r in the (x, z) plane at $y = 7$ km. Rain water is measured in units of g kg^{-1}. (*a*) shows a typical scattered convection pattern whereas (*b*) shows the vertical cloud structure.

side of the u and v equation:

$$-\left(\frac{1}{\tau_u}\bar{u}(z), \frac{1}{\tau_v}\bar{v}(z)\right), \tag{3.1}$$

with relaxation time scales $\tau_u = \tau_v = 4$ h. This type of relaxation is meant to represent the effects of larger-scale atmospheric processes that are not explicitly resolved here but strongly influence the winds on scales of the domain length (Grabowski *et al.* 1996). The relaxation keeps the wind shear weak, and thus the clouds are expected to stay unorganized. The lack of organization is evident in the vertically averaged rain water $\langle q_r \rangle(x, y)$ shown at time $t = 4.8$ h in figure 6(*a*). The clouds form in clusters in different parts of the domain, but no coherent structure develops in this simulation. The horizontal extent of the clouds is roughly 15 km, and the largest

values of rain water (after the vertical average) are roughly 3 g kg^{-1}. Figure 6(b) shows (x, z) contours of the rain water q_r at $y = 7$ km, $t = 4.8$ h, which exhibits the vertical structure of the clouds at a particular y slice. The height of the tallest cloud in this snapshot is roughly 9 km. The heaviest rain is observed to be approximately 9 g kg^{-1}.

3.2. *Squall lines*

To create an environment favourable for squall line formation, the zonal velocity u is initially u_{bg} given by Majda & Xing (2010):

$$u_{bg}(z) = \begin{cases} a(\cos(\pi z/H_0) - \cos(2\pi z/H_0)) & \text{if } z < H_0 \\ -2a & \text{otherwise,} \end{cases} \tag{3.2}$$

where $H_0 = 12$ km, and $a = 11.11$ m s^{-1} (see figure 7). This $u_{bg}(z)$ is similar to the tropical jets in which squall lines often form, and the low-altitude shear should create an eastward-propagating squall line (Lucas *et al.* 2000). Thereafter, the following source term is added to the (u, v) momentum equations in order to keep $\bar{\boldsymbol{u}}_h(z)$ close to $(u_{bg}(z), 0)$:

$$\left(-\frac{1}{\tau_u}(\bar{u}(z) - u_{bg}(z)), -\frac{1}{\tau_v}\bar{v}(z) \right). \tag{3.3}$$

As in the scattered convection runs, the relaxation time scales are chosen as $\tau_u = \tau_v = 4$ h, similar to the value of 2 h that is typically used (e.g. Grabowski *et al.* 1996). Section 6.1 explores the sensitivity to τ_u, τ_v in 2D simulations. Since we initiate with random perturbations in the potential temperature field, there is a spin-up time of approximately 5–10 h during which the convective organization takes place. Relaxation to the background wind is necessary at least during the spin-up time because random convection will tend to reduce the shear that, in nature, would be maintained by larger-scale processes not represented explicitly in our simulations. It may be possible to increase the relaxation time after spin-up, or eliminate Rayleigh damping altogether, but we chose to keep the relaxation parameter fixed throughout any given run for simplicity. Figure 8 shows the horizontal mean of the horizontal velocity components $\bar{u}(z)$ and $\bar{v}(z)$ at $t = 0, 46$ h. Deviation in $\bar{u}$ from the background zonal profile u_{bg} results from convective momentum transport, however, we observe only very small variations in $\bar{v}$ from zero.

The organization of the clouds is observed in the contours of the vertically averaged rain water $\langle q_r \rangle(x, y)$ shown in figure 9(a) (the figure has been shifted to locate the squall line at the centre of the domain). A very clear coherent structure is aligned with the y direction. The direction of propagation cannot be seen in one snapshot, but it will be shown below that the squall line propagates eastward in the line-normal direction. The horizontal extent of the squall line is roughly 40 km. This is smaller than in CRMs with warm-rain microphysics or ice microphysics (see Figure 5 of Wu & Moncrieff (1996)), and it is consistent with decreasing size as microphysical time scales decrease. The strongest clouds here have local values of vertically averaged rain water approximately 2 g kg^{-1}. Negative fluctuations of the potential temperature beneath the squall line (at low altitudes) represent the so-called cold pools, a characteristic feature of squall lines (Fovell & Ogura 1988; Houze 2004). Contours of the potential temperature fluctuation θ'' at $z = 0.4$ km are shown in figure 9(b). Negative fluctuations are observed underneath the squall line, which delimits the cold
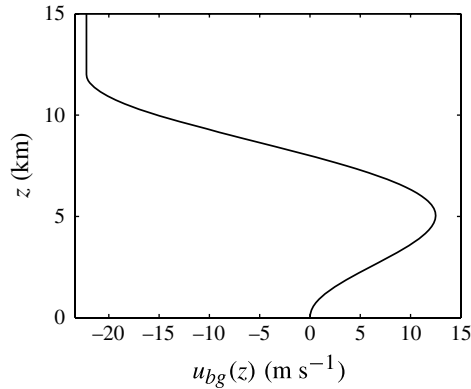
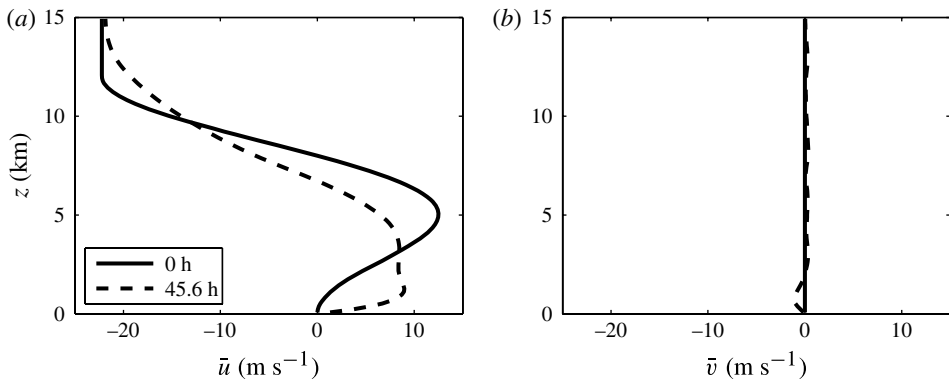FIGURE 7. Velocity background $u_{bg}(z)$ used in the squall line simulations.

FIGURE 8. Three-dimensional FARE model simulation. The solid lines are the background zonal (*a*) and meridional (*b*) profiles. The dotted lines are the horizontal means $\bar{u}(z)$ (*a*) and $\bar{v}(z)$ (*b*) at $y = 64$ km at time $t = 46$ h.

pool. The strongest area of the cold pool (white) is located underneath the heaviest rain.

Another characteristic of squall lines is the typical tilted pattern in the vertical structure of the organized clouds (Fovell & Ogura 1988; Houze 2004). As warm, moist air rises, it condenses and moves to the back of the cloud, resulting in a tilted rain-water profile. Figure 10(*a*) shows the (x, z) contours of rain water q_r at $y = 103$ km, $t = 14.4$ h. A striking tilted profile can be identified, where the heaviest rain is observed toward the front of the squall line and the intensity decays toward the rear of the squall line. Moderate rain between 3 and 6 g kg^{-1} is observed up to 8 km high. However, the cloud may reach 10 km high with weak rain between 0.1 and 3 g kg^{-1}. The (u'', w) vector field is shown in the same plot: a very clear circulation pattern emerges, which is also typical (Wu & Moncrieff 1996). We observe strong winds at the bottom of the clouds, towards the front of the squall line, in the line-normal direction. Updrafts are present near the heavy rain and downdrafts develop toward the back of the clouds. In the vector field anomaly, maximum zonal and vertical velocities reach 20 m s^{-1}. Figure 10(*b*) shows the potential temperature
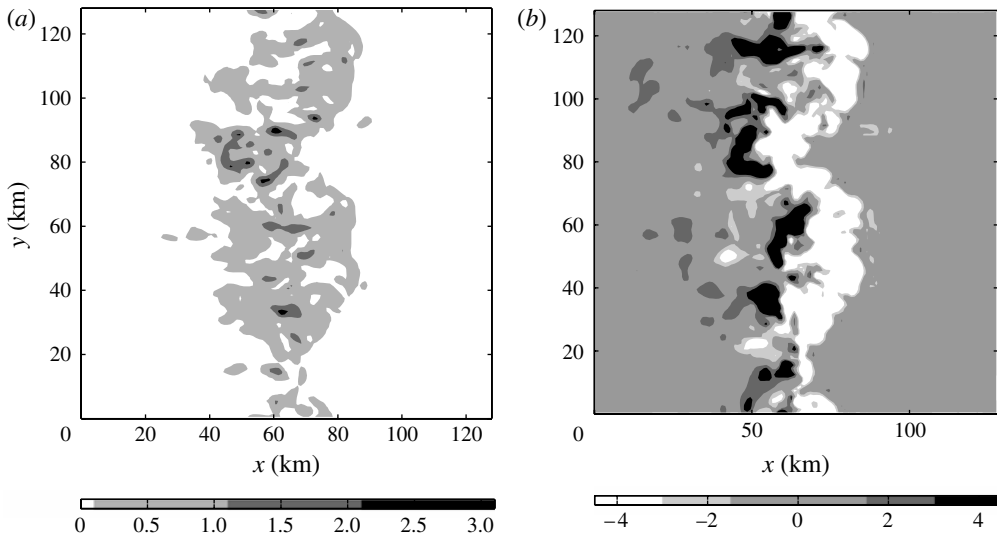
FIGURE 9. Organization of the clouds in a squall line simulation using the 3D FARE model. The clouds have been organized by the background wind of figure 8 and the squall line is moving to the right in the positive x-direction. (*a*) Contours of the vertically averaged rain water $\langle q_r \rangle (x, y)$ in g kg^{-1} at $t = 14.4$ h. (*b*) Contours of the potential temperature fluctuation θ'' in Kelvin at $z = 0.4$ km.

fluctuation from its horizontal mean, θ'', where the cold pool underneath the cloud is evident. Strong winds in the line-normal direction are present inside the cold pool, indicating that the cold air forces the warm less dense air to move upwards. The potential temperature anomaly from its horizontal mean inside the cold pool is approximately -3 K, and the height of the cold pool is roughly 2 km. The tilted profile is also noticeable in the vertical structure of θ''.

We now test whether the FARE model captures the propagation of a squall line as in nature (e.g. LeMone *et al.* 1998; Houze 2004). The coherent structure is expected to propagate in the line-normal direction with speed corresponding to the maximum line-normal velocity, i.e. the maximum horizontally averaged, horizontal velocity max $\bar{u}_h(z)$ (Jorgensen, LeMone & Trier 1997; LeMone *et al.* 1998). In the present setting, $\bar{u}_h(z)$ is relaxed towards $(u_{bg}(z), 0)$, with $du_{bg}(z)/dz > 0$ at low altitudes and thus the squall line is expected to propagate eastward. The direction and speed of propagation can be measured using (x, t) contours of the vertically averaged rain water $\langle q_r \rangle (x, y, t)$ at a particular value of $y = y_0$, e.g. figure 11(*a*) for $y_0 = 64$ km. As expected, the clouds move to the right (eastward). The dotted line has slope equal to the time-averaged maximum $\bar{u}$ during the time window [12, 24] h, and agrees well with the squall line propagation speed. After the spin-up time, the propagation speed of the squall line does not significantly vary during the simulation. Figure 11(*b*) shows the potential temperature fluctuation from its x average at $y = 64$ km. The cold pool is always located underneath the squall line and propagates with the squall line. The bottom plot shows (x, z) contours of the time-averaged rain water during the time window of [22, 24] h. The time average was taken in the frame of reference of the squall line by first subtracting the approximate speed of propagation to obtain a quasi-steady squall line, and then averaging in time. The time-averaged (u'', w) vector field shows
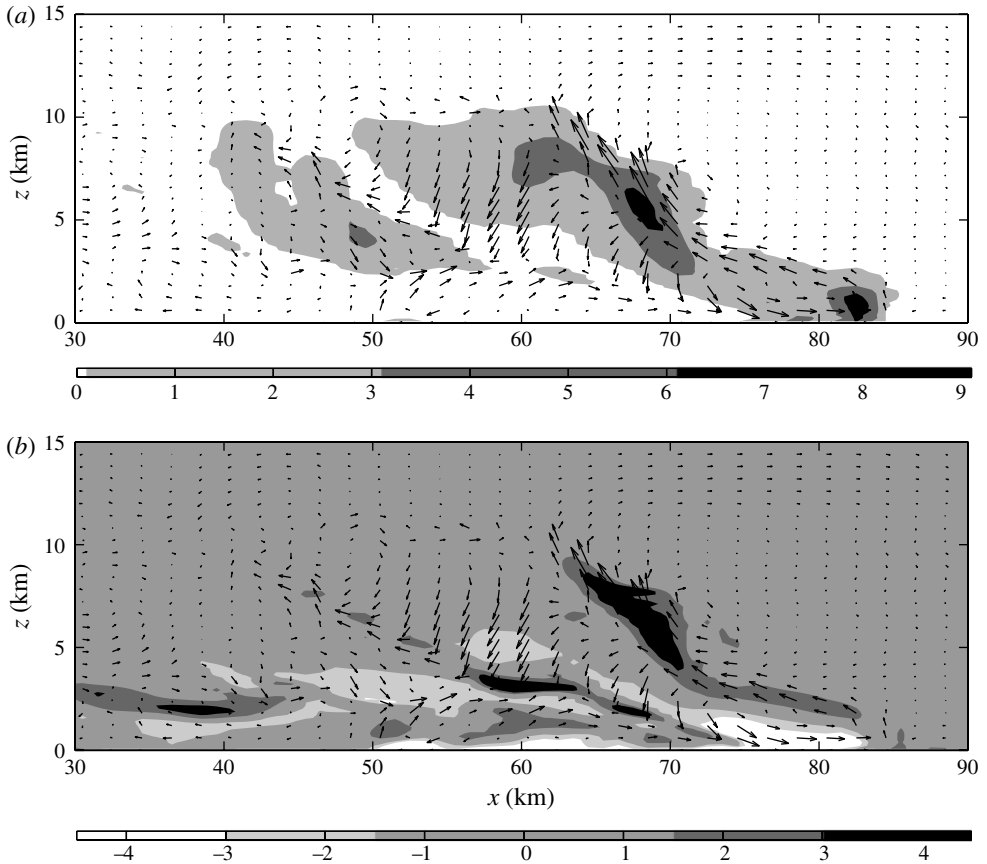
FIGURE 10. Vertical structure of the FARE model squall line and its cold pool are shown. (*a*) Contours of rain water q_r in g kg^{-1} at $y = 103$ km, $t = 14.4$ h. (*b*) Contours of the potential temperature fluctuation θ'' in Kelvin at $y = 103$ km, $t = 14.4$ h. The corresponding (u'', w) vector field is also shown in both plots. Maximum zonal and vertical velocities of 20 m s^{-1} are observed. The clouds have been shifted to the centre of the subdomain [30 km, 90 km] $\times$ [0 km, 15 km].

clear updrafts and downdrafts with the circulation pattern typical of squall lines. The horizontal extent of the tilted profile is roughly 60 km.

4. Numerical results for the 3D FA model

The two settings used in §3 for scattered and organized convection are here investigated using the 3D FA model. The condensation and evapouration time scales chosen in this section are $\tau_c = 2.25$ min and $\tau_e = 13.5$ s. We have found that the FA model is sensitive to the condensation and evapouration time scales and other parameters used in the simulation. In particular, coherent 3D squall lines were not robust when we used $\tau_c = \tau_e = 2.25$ min as in Majda *et al.* (2010) and Deng *et al.* (2012). Note that the product $\tau_e^{-1} q_*^{-1}$ appears in the expression for evapouration (2.14), and the reference value q_* has been chosen as $q_* = 0.01$ kg kg^{-1}. Alternatively, q_* could have been decreased with τ_e held fixed, so it may be more appropriate to interpret our results in terms of decreasing the product $\tau_e^{-1} q_*^{-1}$, rather than in terms of
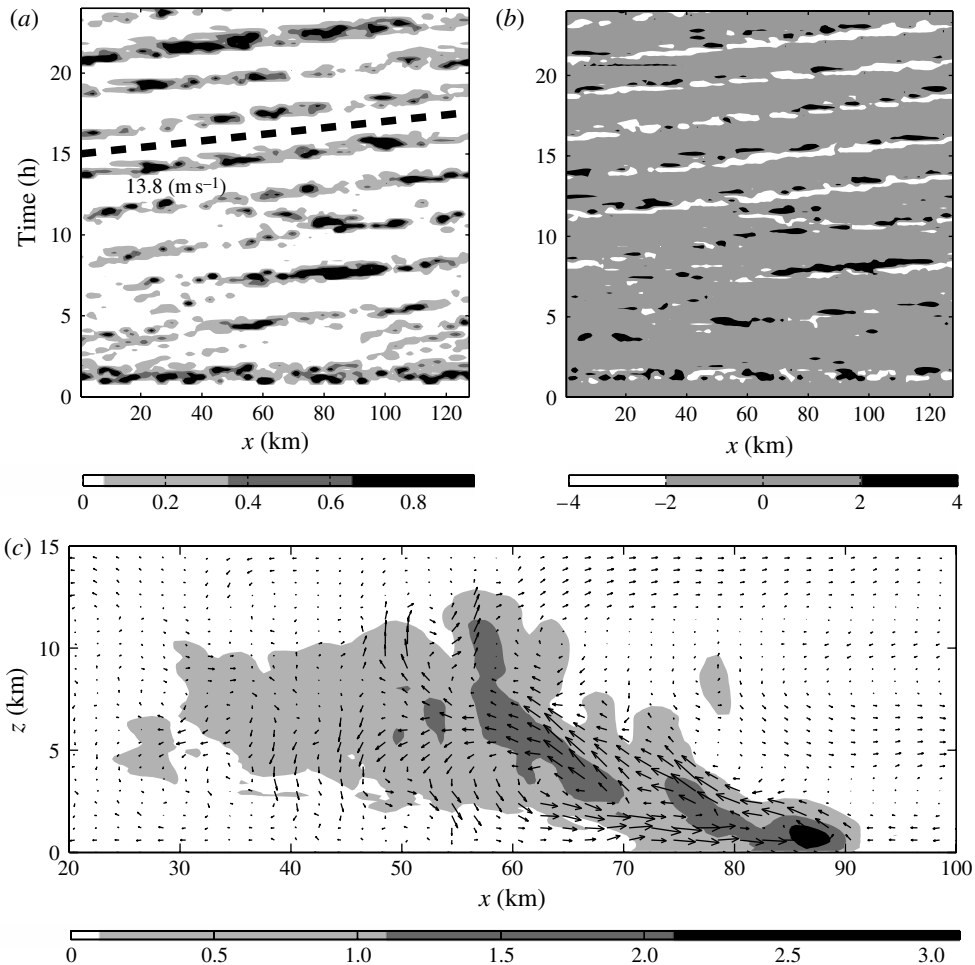
FIGURE 11. The propagation of the FARE model squall lines and the vertical structure of the time averaged rain water are shown here. (*a*) The (x, t) contours of the vertically averaged rain water $\langle q_r \rangle (x, y, t)$ at $y = 64$ km; the line has slope equal to the time-averaged maximum $\bar{u}$ during the time window [12, 24] h. (*b*) The (x, t) contours of θ'' at $z = 0.4$ km. (*c*) Time average of q_r and (u'', w) vector field in a reference frame moving with the squall line.

decreasing τ_e alone. The relaxation time scales for maintaining the background winds are the same as in the previous section using the FARE model, namely $\tau_u = \tau_v = 4$ h.

4.1. *Scattered convection*

The initial conditions are identical to those of § 3.1. Figure 12(*a*) shows $\langle q_r \rangle (x, y)$ at $t = 19.2$ h, at which time scattered convection is clear. The rain water intensity is comparable to that observed with the FARE model in the previous section. The vertical structure of the clouds at $y = 113$ km is exhibited in the (x, z) contours of rain water shown in figure 12(*b*). The height of the tallest cloud here is about 9 km. Note that, while 'cloud water' is not explicit in our models by the assumption of fast autoconversion, we will nevertheless use the terminology 'cloud' for saturated regions with $q_r > 0$, which represent suspensions of sedimenting water drops.
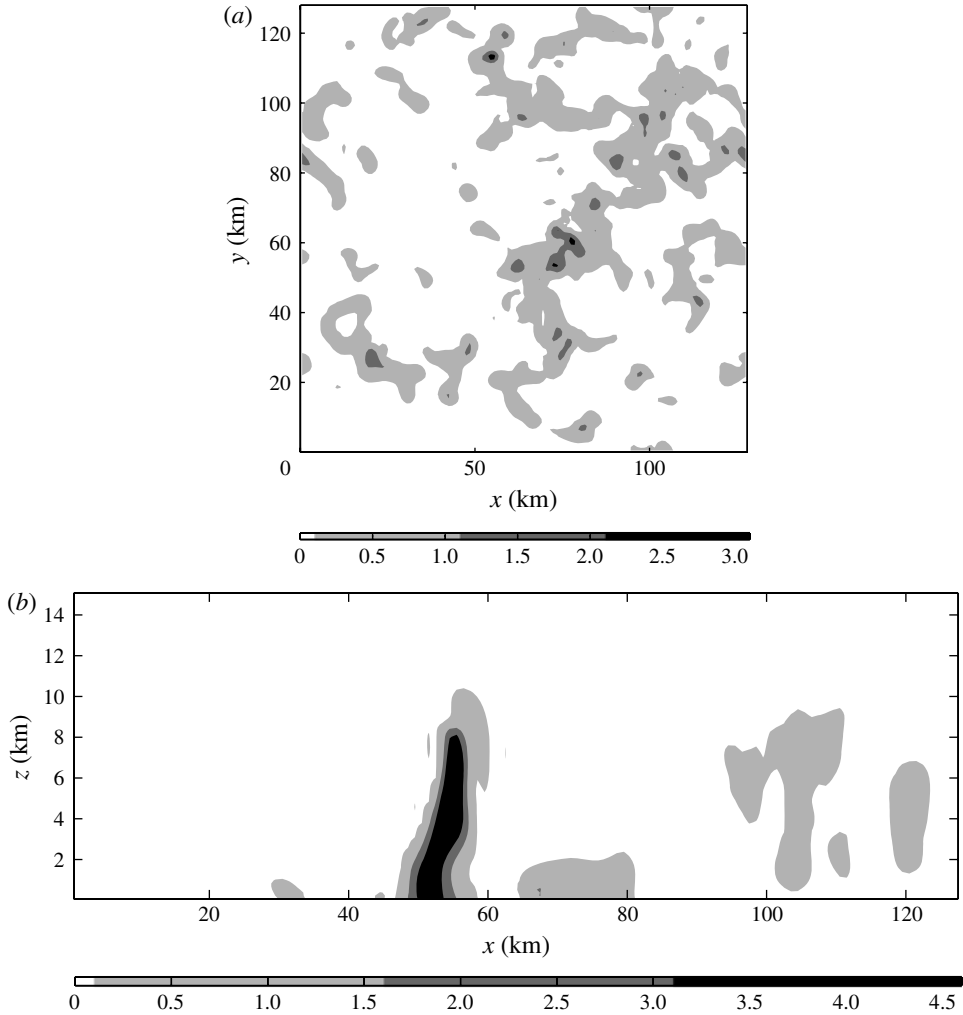
FIGURE 12. Contours of 2D data in a 3D simulation obtained using the 3D FA model. (*a*) Vertically averaged rain water $\langle q_r \rangle(x, y)$ at time $t = 19.2$ h. (*b*) Contours of rain water in the (x, z) plane at $y = 113$ km and $t = 19.2$ h. Rain water is measured in units of g kg^{-1}.

4.2. *Squall lines*

The initial conditions in this simulation are identical to those of § 3.2. Figure 13 for FA is analogous to figure 8 for FARE. The deviations of $\bar{u}$ from the background zonal profile u_{bg} due to convective momentum transport are similar in the two models FA and FARE.

Figure 14(*a*) shows the vertically averaged rain water $\langle q_r \rangle(x, y)$ at $t = 45.6$ h, where the coherent structure is evident. The figure has been shifted to locate the squall line at the centre of the domain. The horizontal extend of the clouds is roughly 50 km, comparable to the extent observed in the FARE simulations. As will be shown below, the clouds propagate eastwards in the line-normal direction maintaining the coherent structure. Fluctuations of the potential temperature from its horizontal mean at low altitudes are shown in figure 14(*b*). Negative values are observed underneath
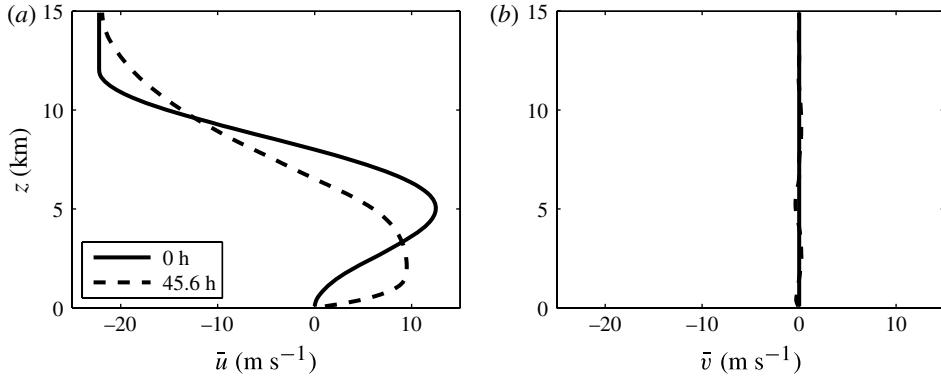
FIGURE 13. Three-dimensional FA model simulation. The solid lines are the background zonal (*a*) and meridional (*b*) profiles. The dotted lines are the horizontal means $\bar{u}(z)$ (*a*) and $\bar{v}(z)$ (*b*) at $y = 64$ km at time $t = 46$ h.
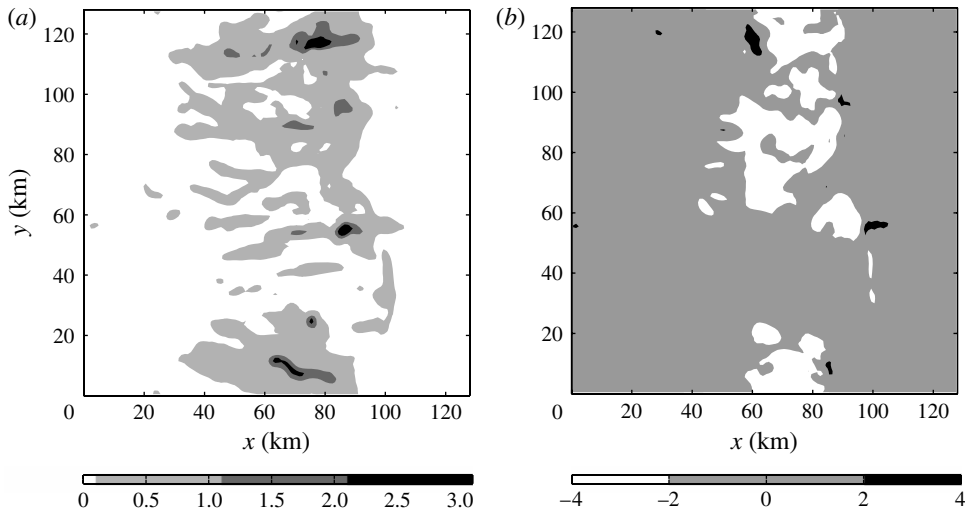

FIGURE 14. Organization of the clouds in a squall line simulation using the 3D FA model. (*a*) Contours of the vertically averaged rain water $\langle q_r \rangle(x, y)$ in g kg^{-1} at $t = 45.6$ h. (*b*) Contours of the potential temperature fluctuation θ'' in Kelvin at $z = 0.4$ km.

the coherent structure, which demonstrates that the FA model captures the cold pool observations.

Figure 15(*a*) shows the (x, z) contours of rain water q_r at $y = 7$ km, $t = 45.6$ h, where a tilted profile and a circulation pattern are observed. The height of the tallest cloud in this snapshot is roughly 11 km. The (x, z) contours of θ'' are shown in figure 15(*b*). Negative fluctuations at low altitudes underneath the cloud detects the position of the cold pool. The height of the cold pool is roughly 1.5 km, comparable to the 2 km observed with the FARE model.

We note that in the present simulation, the spin-up time for the squall line to form was significantly longer than for the FARE model. Although the clouds move to the east, their alignment in the *y* direction is not evident during the first day. In contrast, the alignment in the FARE model was achieved roughly 10 h after the
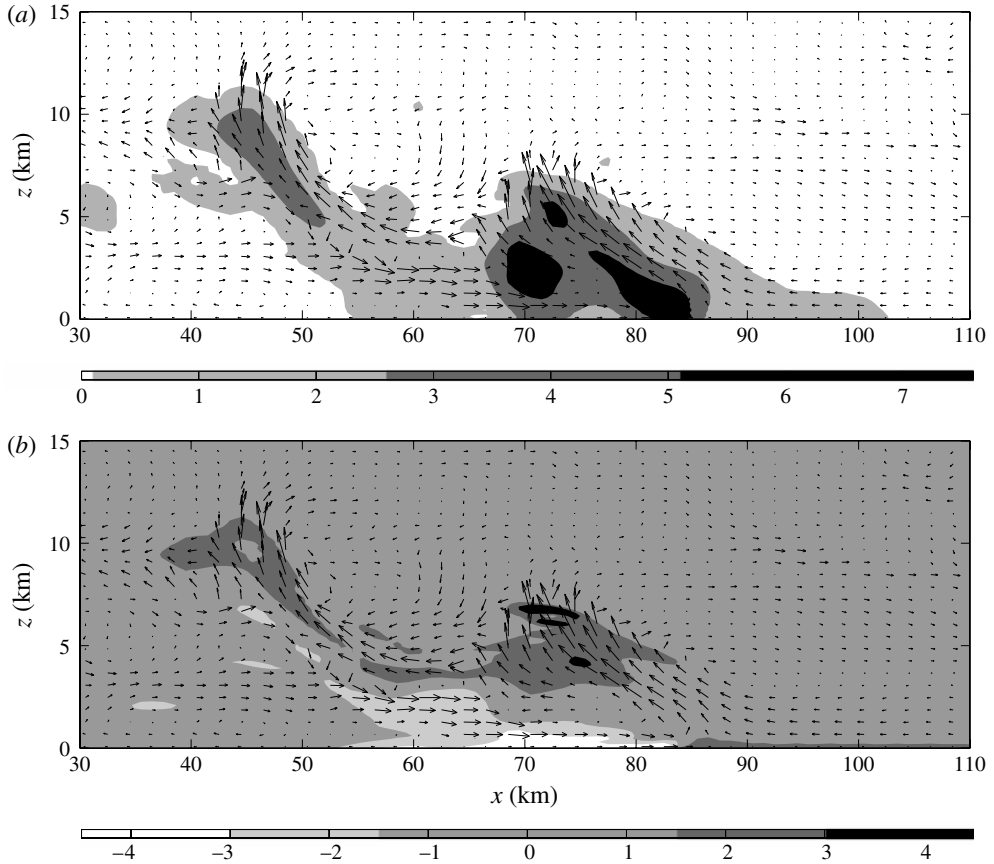
FIGURE 15. Vertical structure of the FA model squall line and its cold pool are shown. (*a*) Contours of rain water $q_r(x, y, z)$ in g kg^{-1} at $y = 7$ km, $t = 45.6$ h. (*b*) Contours of the potential temperature fluctuation θ'' in Kelvin at $y = 7$ km, $t = 45.6$ h. The corresponding (u'', w) vector field is also shown in both plots. Maximum zonal and vertical velocities of 15 m s^{-1} are observed. The clouds have been shifted to the centre of the subdomain [30 km, 110 km] $\times$ [0 km, 15 km].

initial perturbation was introduced. Figure 16 shows the (x, t) contours of the vertically averaged rain water $\langle q_r \rangle$ at $y = 64$ km during the second day figure 16(*a*), when we observe a clear propagating squall line. The dotted line has slope equal to the maximum $\bar{u}$ during the time window [46, 48] h, and agrees well with the squall line propagation speed. Figure 16(*b*) shows the (x, t) contours of the potential temperature fluctuation from its x-average at $y = 64$ km, $z = 0.4$ km. The cold pool always resides underneath the squall line and propagates with the squall line. Similar to figure 11, the bottom plot shows (x, z) contours of the time-averaged rain water during the time window of [31, 33] h. The time-averaged (u'', w) vector field shows clear updrafts and downdrafts with the circulation pattern typical of squall lines.

Lastly, we point out again that the parameter values $\tau_c = 2.25$ min and $\tau_e = 13.5$ s are different from those used by Majda *et al.* (2010) and Deng *et al.* (2012). In particular, coherent 3D squall lines were not robust when we used $\tau_c = \tau_e = 2.25$ min as in Majda *et al.* (2010) and Deng *et al.* (2012). In nature and comprehensive
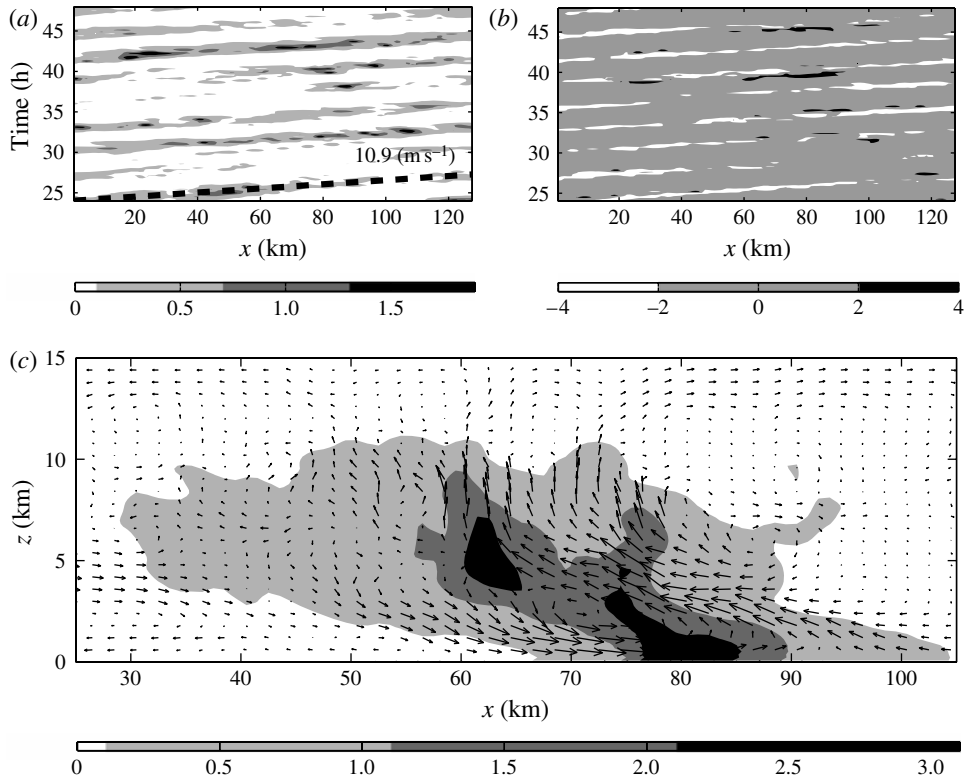
FIGURE 16. Propagation of the FA model squall line and the vertical structure of the time averaged rain water are shown here. (*a*) The (x, t) contours of the vertically averaged rain water $\langle q_r \rangle$ at $y = 64$ km during the second day; the line has slope equal to the time-averaged maximum $\bar{u}$ during the time window $[46, 48]$ h. (*b*) The (x, t) contours of θ'' at $y = 64$ km, $z = 0.4$ km. (*c*) Time average of q_r and (u'', w) vector field in a reference frame moving with the squall line.

CRMs, the rain evapouration time scale τ_e is actually longer than the condensation time scale τ_c, and the autoconversion time scale is also longer than τ_c. In a model where the autoconversion time scale has been taken to be zero, it is not necessarily the case that realistic values of τ_e and τ_c produce a realistic squall line. Our results suggest that, for squall lines, if the autoconversion time scale is taken to zero, then the other microphysical time scales should be taken to zero for consistency. One may speculate as to why the squall line results are more sensitive to τ_e than the Majda *et al.* (2010) and Deng *et al.* (2012) studies of individual convective towers and their merger. A longer evapouration time scale will lead to less evapourative cooling as rain falls behind the leading edge of the squall line. Less cooling in turn leads to reduced downdrafts and a weaker cold pool behind the squall line, and thus less of the characteristic tilted circulation pattern. The sensitivity to τ_c and τ_e is explored in 2D simulations in the next section.

5. Comparison of the FARE and FA models in 2D

The FARE model was obtained from the FA model by assuming fast condensation and evapouration of rain. The FARE model can therefore be seen as the limit of FA as
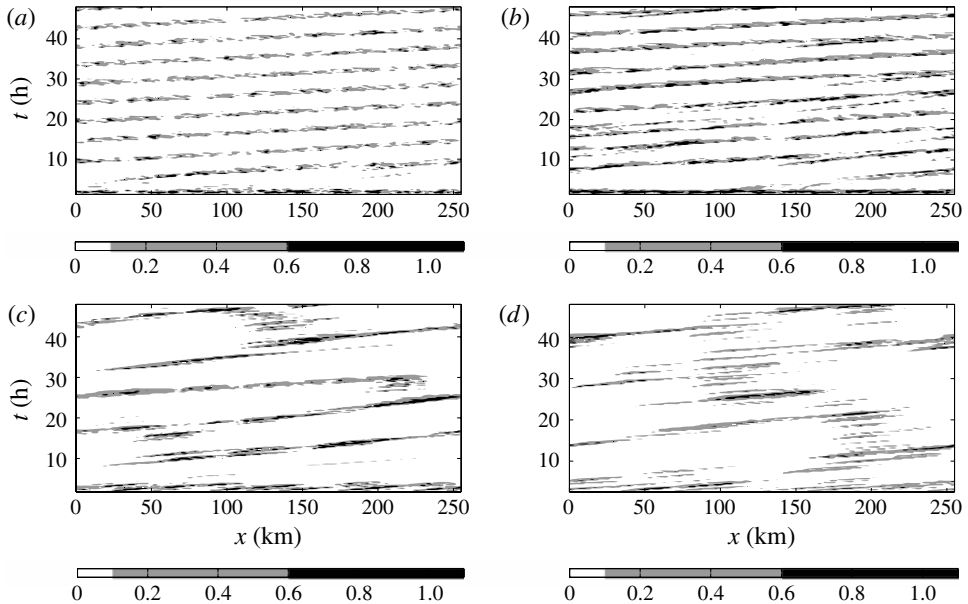
FIGURE 17. A comparison of results obtained with the 2D FARE model and the 2D FA model with different values of τ_c and τ_e. The squall line propagation is shown for the 2D FARE model (*a*), and the 2D FA model with $\tau_c = \tau_e = 0.225$ min (*b*), $\tau_c = \tau_e = 2.25$ min (*c*) and $\tau_c = \tau_e = 6.75$ min (*d*).

the time scales τ_c, τ_e due to condensation and rain evapouration go to zero,

$$\text{FARE} = \lim_{\tau_c, \tau_e \to 0} \text{FA}. \qquad (5.1)$$

As a result, we must anticipate that the FA model behaves similarly to FARE as τ_c and τ_e decrease. This is investigated in this section using 2D simulations. The (x, z) domain size is 256 km × 15 km, which is twice as long as, yet comparable to, the 3D simulations in §§ 3 and 4, and the moistening and cooling rates have accordingly been reduced by a factor of two.

Figure 17 shows the (x, t) contours of the vertically averaged rain water $\langle q_r \rangle (x, t)$ in g kg^{-1} from 0 to 48 h, using the 2D FARE model (figure 17*a*), and the 2D FA model with $\tau_c = \tau_e = 0.225$ min (figure 17*b*), $\tau_c = \tau_e = 2.25$ min (figure 17*c*) and $\tau_c = \tau_e = 6.75$ min (figure 17*d*). The values of $\tau_c = \tau_e = 0.225$ min give the closest qualitative results to FARE. For instance, the squall lines are more uniform and coherent as we decrease τ_c and τ_e. The larger values of τ_c and τ_e produce intermittent squall lines. The same initial random perturbation in the potential temperature has been used in all four cases.

As another comparison, figure 18 shows the vertical structure of the clouds obtained with the 2D FARE model (figure 18*a*), and by the 2D FA model with $\tau_c = \tau_e = 0.225$ min (figure 18*b*), $\tau_c = \tau_e = 2.25$ min (figure 18*c*) and $\tau_c = \tau_e = 6.75$ min (figure 18*d*). The case with $\tau_c = \tau_e = 0.225$ min has a tilted profile similar to that of 2D FARE. The bigger values of τ_c and τ_e in the FA model produce less tilted profiles.

To quantify these comparisons, a measurement of the tilt is provided by the vertical transport of horizontal momentum, $\overline{u'' w''}$. A time average of this quantity (not shown)
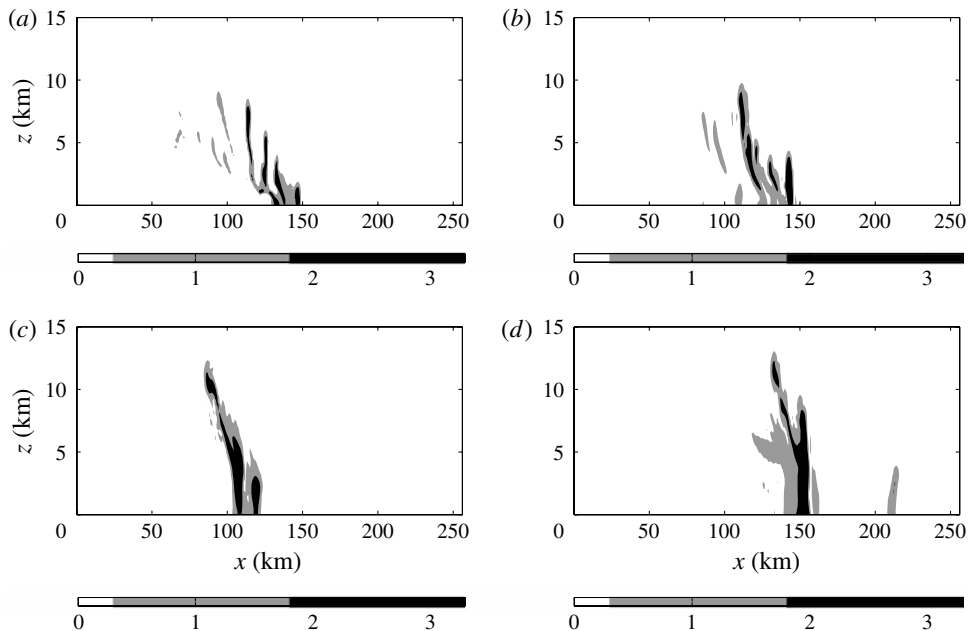
FIGURE 18. Another comparison between the FARE and FA models. Snapshots of rain water $q_r(x, z)$ contours with the 2D FARE model (*a*), and the 2D FA model with $\tau_c = \tau_e = 0.225$ min (*b*), $\tau_c = \tau_e = 2.25$ min (*c*) and $\tau_c = \tau_e = 6.75$ min (*d*).

during the last 12 h of the second day has absolute maxima of 0.16, 0.26, 1.7 and 1.9 m^2 s^{-2} for the 2D FA model with decreasing time scales and the FARE model, respectively. The larger values of $\overline{u''w''}$ correspond to the visually larger tilts in figure 18 for the FARE model and for the FA model with smallest τ_c and τ_e. Furthermore, the values of $\bar{u}(z, t)$ at $t = 48$ h (not shown) display a similar trend for τ_c and τ_e values: the FARE model and $\tau_c = \tau_e = 0.225$ min FA model have similar $\bar{u}(z)$ values, whereas the $\bar{u}(z)$ profiles for the other two FA cases are different from the FARE results. More precisely, the normalized L^1 norm of the difference between the FARE model and each of the FA results is 1.3, 1.3 and 0.2 m s^{-1} in order of decreasing $\tau_c = \tau_e$. In short, the FA results with $\tau_c = \tau_e = 0.225$ min are similar to the FARE model results, whereas the FA results with $\tau_c = \tau_e = 2.25$ min show significant differences from the FARE model results.

6. Sensitivity studies in two dimensions

In this section, the 2D FARE model will be used to show the sensitivity or robustness of the results to variations in the model parameters, such as relaxation time scales, rainfall velocity, usage of sponge layers and moistening and cooling rates with larger domain sizes. It will be shown that in all cases the organized convection always occurs regardless of the parameter changes, but the detailed characteristics will vary from case to case.

6.1. *Sensitivity to the relaxation time scales τ_u and τ_v*

In this section, we study the sensitivity of the numerical results to the relaxation time scales τ_u and τ_v of $\bar{\boldsymbol{u}}_h(z)$ towards the horizontal velocity background $(u_{bg}(z), 0)$.
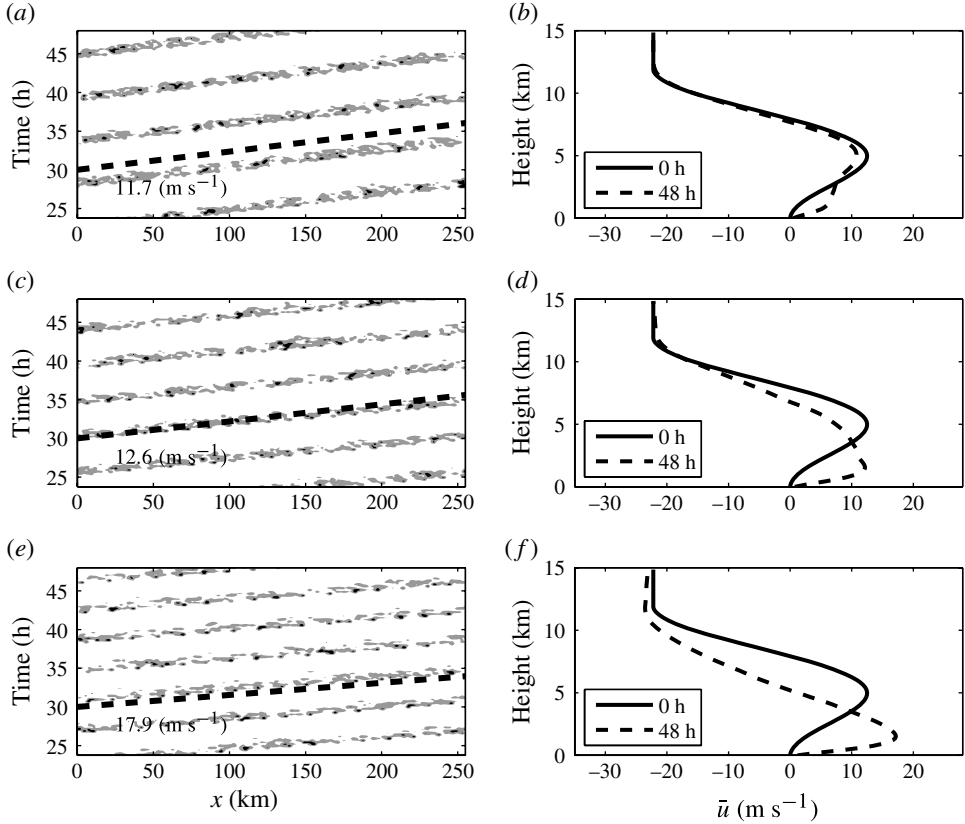
FIGURE 19. A comparison of different momentum relaxation times, τ_u, in the squall line simulation implemented by the FARE model: (a,b) $\tau_u = 1$ h; (c,d) $\tau_u = 4$ h; (e,f) $\tau_u = 24$ h. (a,c,e) Contours of vertically averaged rain water $\langle q_r \rangle(x,t)$ in g kg^{-1} and a dashed line with slope the maximum line-normal velocity are shown. The same greyscale as in figure 17 has been used here. (b,d,f) Horizontal mean of the zonal velocity $\bar{u}(z)$ in m s^{-1} is shown at different times.

This relaxation is intended to maintain the horizontal mean of the horizontal velocity $\bar{\boldsymbol{u}}_h(z)$ close to the initial background. Figure 19 shows a comparison of $\tau_u = 1$ h (a,b), $\tau_u = 4$ h (c,d) and $\tau_u = 24$ h (e,f). The first column shows the propagation of the squall line during the second day in each case. In all cases squall lines are always observed. However, the speed of propagation varies as the zonal velocity $\bar{u}(z)$ may vary from its initial value for larger τ_u values. Included in each plot is a dashed line with slope given by the maximum line-normal velocity averaged from $t = 24$ to 48 h. These dashed lines roughly follow the speed of propagation of the squall line in each case, in agreement with the propagation of observed squall lines (LeMone *et al.* 1998).

6.2. *Sensitivity to the fall velocity V_T*

We now use different values of the rain fall velocity V_T to study the sensitivity of the results to this parameter, as shown in figure 20. Figure 20(a,c,e) shows the (x, z) contours of rain water, where the locations of the clouds have been shifted to the centre of the domain for visual clarity. Note that, while 'cloud water' is not explicit in our models by the assumption of fast autoconversion, we will nevertheless use the
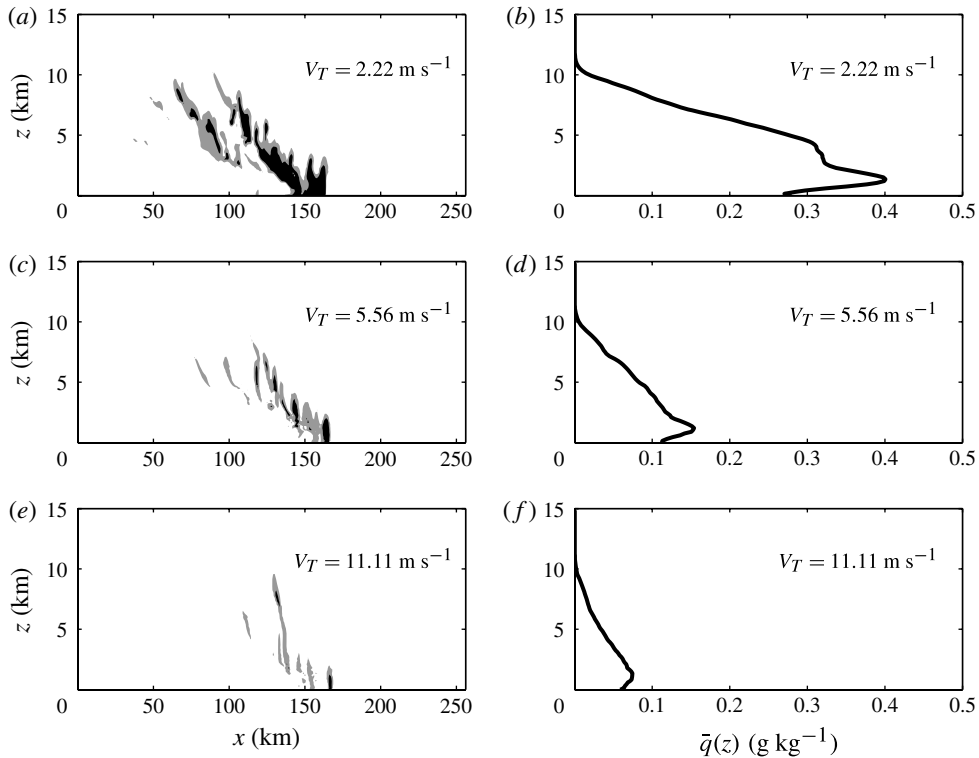
FIGURE 20. A comparison of the 2D FARE results with different fall velocities V_T is presented here: (a,b) $V_T = 2.22$ m s^{-1}; (c,d) $V_T = 5.56$ m s^{-1}; (e,f) $V_T = 11.11$ m s^{-1}. (a,c,e) Contours of $q_r(x, z)$ in g kg^{-1} at $t = 39$ h. (b,d,f) The (x, t) averaged rain water as a function of z. The same greyscale contours as figure 18 are used here.

terminology 'cloud' for saturated regions with $q_r > 0$, which represent suspensions of sedimenting water drops. Figure 20(b,d,f) shows the (x, t) averaged rain water as a function of z, for $V_T = 2.22$ m s^{-1} (a,b), $V_T = 5.56$ m s^{-1} (c,d) and $V_T = 11.11$ m s^{-1} (e,f). These are typical terminal velocities for rain drops with diameters of roughly 1–10 mm (Pruppacher & Klett 1997). For larger values of V_T, the averaged rain water is smaller, which is consistent with the role of V_T in removing water from the domain or bringing it to lower levels where it may evapourate if the air is unsaturated. While V_T does affect the average rain amount, the presence of squall lines with tilted profiles is not sensitive to this parameter.

6.3. *Comparison with usage of sponge layers*

It is customary in atmospheric simulations to use a 'sponge layer' near the top boundary (e.g. Grabowski *et al.* 1996). The purpose of this is to damp vertically propagating gravity waves that may otherwise reflect off the artificial rigid lid at the top boundary. Since our goal is to keep the model as simple as possible, no sponge layers have been used in the previous numerical results. In this section, we investigate the sensitivity of the results to the presence of a sponge layer.

In the sponge layer setting, a linear drag term is added to the equations for all variables: $-d_s(z)u$, $-d_s(z)\theta$, etc. The damping rate $d_s(z)$ varies as a function of z and is non-zero only for $z > 10$ km. For the sponge layer 10 km $< z <$ 15 km, it is
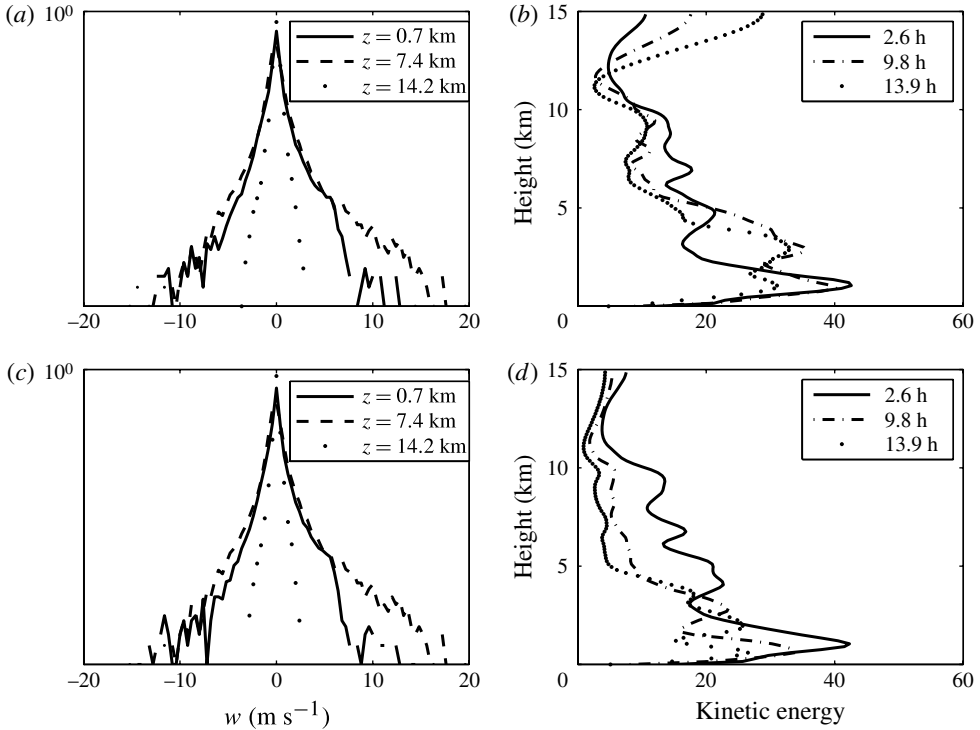
FIGURE 21. The sensitivity of the numerical results to sponge layers is shown. (a,b) No sponge layer. (c,d) Sponge layer implementation. (a,c) Probability distribution functions of the vertical velocity at $z = 0.675$ km, $z = 7.4$ km and $z = 14.2$ km. (b,d) Total kinetic energy at different times, averaged over x at each z level.

a square sinusoidal function that vanishes at $z = 10$ km and reaches its maximum of $(1\ \mathrm{h}^{-1})$ at the top boundary $z = 15$ km.

Figure 21 shows results with the 2D FARE model without (a,b) and with (c,d) a sponge layer. Figure 21(a,c) shows probability distribution functions (p.d.f.s) of vertical velocity at different heights: $z = 0.675$ km (solid line), $z = 7.4$ km (dashed line) and $z = 14.1$ km (dotted line). The distributions do not appear to be affected by the presence or absence of a sponge layer. This suggests that the sponge layer may be omitted for the sake of simplicity if one is concerned with only broad features such as the presence or absence of an organized squall line or its p.d.f. of vertical velocity. Nevertheless, the sponge layer may be important for certain studies, and its effect can be seen in the kinetic energy profiles in figure 21(b,d). The times selected in the last column were carefully chosen to exhibit the largest kinetic energy in the uppermost levels. These snapshots show that the kinetic energy is reduced in the sponge layer $10\ \mathrm{km} < z < 15\ \mathrm{km}$, whereas the levels below $z = 10$ km are affected less, if at all. The statistical comparisons in figure 21 corroborate the visual similarity of the squall lines in the two cases (not shown).

6.4. *Sensitivity to domain size and cooling and moistening rates*

In atmospheric simulations, it is customary to apply horizontally uniform moistening and cooling forcing when the set-up uses a limited domain size with periodic boundary
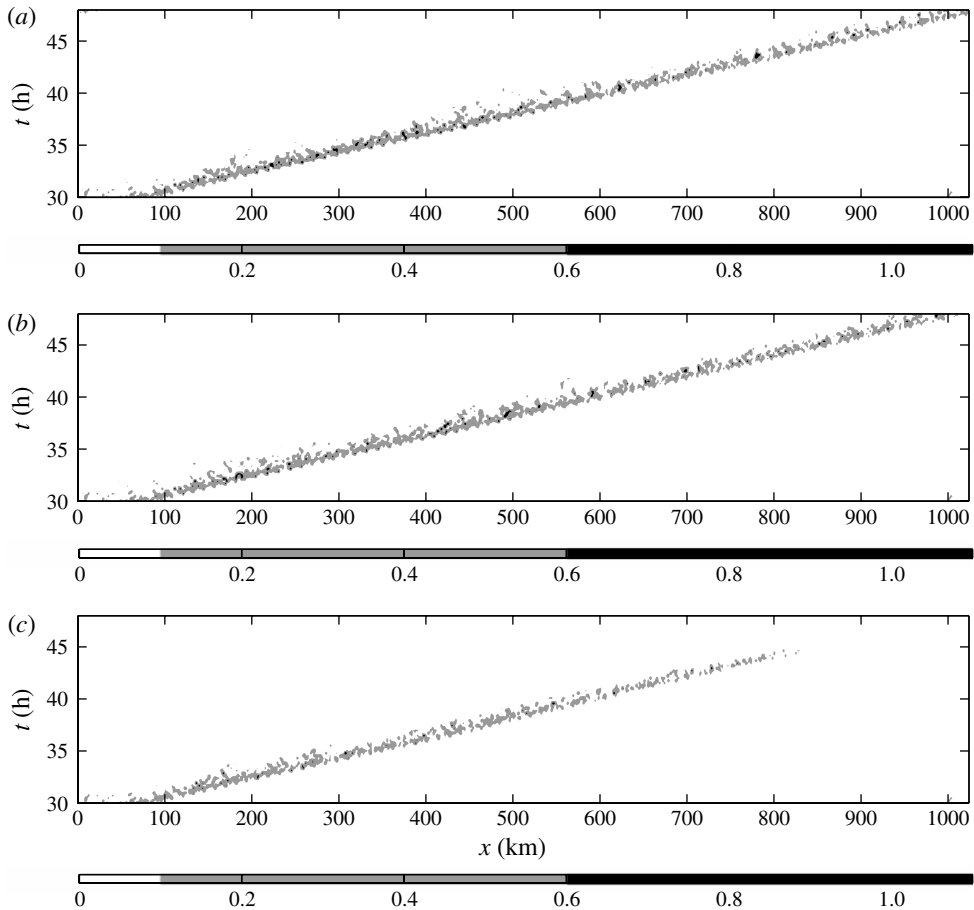
FIGURE 22. Large-domain simulations with reduced moistening and cooling rates. (*a*) Both moistening and cooling implemented for the whole 2-day simulation. (*b*) The cooling is turned off after 30 h, while keeping the moistening rate. (*c*) Both cooling and moistening are turned off after 30 h.

conditions (e.g. Grabowski *et al.* 1996; Jung & Arakawa 2005). This forcing is meant to represent the effects of larger-scale phenomena, such as moisture convergence due to larger-scale waves, on the simulated domain, and the form of the forcing could be motivated by observational measurements (Grabowski *et al.* 1996). Such a forcing has been employed here due to the limited size of the 3D domain from limitations of computational expense. In this section, we perform simulations on a larger 2D domain, with reduced moistening and cooling rates, in order to test whether the limited domain size affects the simulated squall lines. Furthermore, we investigate the individual effect of the cooling rate and of the moistening rate.

In this sensitivity study, we now use a domain of size 1024 km × 15 km, and the cooling and moistening rates have been reduced accordingly by a factor of 8 from that used in the 3D simulations with 128 km wide domain. The maximum moistening rate becomes then 2.1 g kg^{-1} and the maximum cooling rate $\sim$3 K day^{-1}.

Figure 22 shows contours of the vertically averaged rain water $\langle q_r \rangle (x, t)$ for three cases. In the top plot, the moistening and cooling are both applied during 2 days.

A longer spin-up time of roughly 5 h is observed (not shown) due to the smaller moistening rate. In the middle plot, both the moistening and cooling are applied during the first 30 h, but then the cooling is turned off thereafter while maintaining the moistening. In this case, the squall line keeps propagating as a free wave similarly to the previous case (only shown from 30 to 48 h). Finally, the bottom plot shows the results when both the moistening and cooling are turned off at time $t = 30$ h. In this case, the squall line vanishes roughly 13 h after the forcing is turned off. These three cases demonstrate that the squall lines in the FARE model still form when much smaller moistening and cooling rates are used with a larger domain. In addition, the cooling is not essential for the maintenance of the squall line, whereas the moistening is needed in this set-up. The cooling is likely not essential here because the simplified form of the saturation water vapour, $q_{vs}(z)$, is independent of the temperature in this minimal set-up.

7. Conclusions and discussion

Two minimal models for precipitating organized convection were formulated and tested using numerical simulations. It was shown that, under appropriate environmental conditions, both models capture two basic regimes of precipitating convection: unorganized scattered convection and organized propagating squall lines. Scattered convection results when the background winds are weak; squall lines arise in the presence of low-altitude shear in the background wind. Commonly observed features of squall lines are faithfully captured by the minimal models, including tilted cloud profiles, low-altitude cold pools and propagation speed approximately equal to the maximum line-normal velocity at lower altitudes. The ability of the models to capture these broad features of squall lines indicates insensitivity of such features to the detailed microphysics of phase changes.

The main simplifications that are common to both the FA and FARE models are an assumption of a Boussinesq atmosphere and fast autoconversion of cloud water to rain water. With these simplifications, evolution equations for only water vapour and rain water are retained to represent warm-rain bulk cloud physics. A design principle is that the inviscid forms of the models conserve equivalent potential temperature θ_e, rain-water potential temperature θ_r and total water q_t, which is likely part of the reason they are able to capture realistic tropical dynamics.

In addition to fast autoconversion, the FARE model assumes fast evapouration of rain water to form water vapour and fast condensation of water vapour to form rain water. Our simulations suggest that the FARE model is more robust than the FA model. While the FA model is fairly robust for unorganized convection (as also seen in the earlier work of Majda *et al.* (2010) and Deng *et al.* (2012)), its representation of organized squall lines was seen here to be sensitive to model parameter choices. In other words, the limit of fast autoconversion may yield more robust results if used together with fast rain evapouration (and fast condensation). As a demonstration of consistency of the FA and FARE model formulations, our 2D sensitivity studies show that the FA model behaves more like the FARE model as the relaxation times τ_c, τ_e in the model evapouration and condensation source terms are decreased together toward zero.

A numerical modelling advantage of the FARE model is fewer model parameters: there is no need to specify closures for condensation C_d or evapouration E_r, and thus stiff source terms have been removed. In general we found that the FARE model is less sensitive than FA to parameters such as domain size, moistening and cooling

rates and viscosity coefficients. The FARE model also has the additional conservation principle for total energy in (2.39), and implications of (2.39) will be a topic of further investigation. Finally, we expect that the simplicity and conservation properties of the FARE model may provide a starting point for theoretical analyses. In particular, our future plans include analysis of 2D versus 3D squall lines toward understanding and characterizing 3D convective momentum transport (Moncrieff 1992; Majda & Stechmann 2008, 2009; Khouider *et al.* 2012).

Acknowledgements

Appendix A. Derivation of the approximate water vapour at saturation

The particular choice of $q_{vs}(z)$ from figure 3 is derived in the following way. The thermodynamic formula for q_{vs} is a function of pressure p and temperature T:

$$q_{vs}(p, T) = \frac{R_d}{R_v} \frac{e_s(T)}{p}. \quad (A\,1)$$

In this formula, e_s is the partial pressure due to water vapour under saturated conditions, and $e_s(T)$ is found from the Clausius–Clapeyron relation (Rogers & Yau 1989; Houze 1993; Emanuel 1994; Pruppacher & Klett 1997)

$$e_s(T) = e_{s,o} \exp\left(-\frac{L}{R_v}\left(\frac{1}{T} - \frac{1}{T_o}\right)\right), \quad (A\,2)$$

where $e_{s,o} \approx 3500$ kg m^{-1} s^{-2} is the saturation water-vapour pressure at the surface, with surface temperature $T_o \approx 300$ K. As described in §2.2, an approximate form of $q_{vs}(z)$ can be determined for an anelastic atmosphere:

$$q_{vs}(p, T) \approx q_{vs}(\tilde{p}(z), \tilde{T}(z)) \equiv q_{vs}(z). \quad (A\,3)$$

Hence a specific form of $q_{vs}(z)$ can be determined from (A 1)–(A 3) if profiles $\tilde{p}(z)$ and $\tilde{T}(z)$ are given. These are chosen here by the requirements of an ideal gas law, $\tilde{p} = \tilde{\rho} R_d \tilde{T}$, hydrostatic balance, $\mathrm{d}\tilde{p}/\mathrm{d}z = -g\tilde{\rho}(z)$, and a linear background potential temperature, $\tilde{\theta}(z) = \theta_o + Bz$, where $\tilde{\theta}$ is defined as $\tilde{\theta} = \tilde{T}(p_o/\tilde{p})^{R_d/c_p}$. Determining $\tilde{p}(z)$ and $\tilde{T}(z)$ from these relations is done in the following way.

The definition

$$\tilde{\theta}(z) = \tilde{T}(z)\left(\frac{p_o}{\tilde{p}(z)}\right)^{R_d/c_p} \quad (A\,4)$$

can be rewritten, upon using the ideal gas law $\tilde{p} = \tilde{\rho} R_d \tilde{T}$, as

$$\tilde{p}(z) = \tilde{\rho}(z) R_d \left(\frac{\tilde{p}(z)}{p_o}\right)^{R_d/c_p} \tilde{\theta}(z). \quad (A\,5)$$

Then, using (A 5) and hydrostatic balance $\mathrm{d}\tilde{p}(z)/\mathrm{d}z = -g\tilde{\rho}(z)$, one obtains

$$\frac{\mathrm{d}}{\mathrm{d}z}\left[\left(\frac{\tilde{p}(z)}{p_o}\right)^{R_d/c_p}\right] = -\frac{g}{c_p\tilde{\theta}(z)}. \tag{A 6}$$

Assuming a linear background potential temperature $\tilde{\theta}(z) = \theta_o + Bz$, integration of (A 6) yields

$$\frac{\tilde{p}(z)}{p_o} = \left(1 - \frac{g}{Bc_p}\log\left(1 + \frac{Bz}{\theta_o}\right)\right)^{c_p/R_d} \equiv (f(z))^{c_p/R_d}. \tag{A 7}$$

Thus, an approximation to the water vapour saturation profile q_{vs} is

$$q_{vs}(z) = \frac{q_{vs,o}}{\tilde{p}(z)/p_o}\exp\left[-\frac{L}{R_v}\left(\frac{1}{f(z)(\theta_o + Bz)} - \frac{1}{\theta_o}\right)\right] \tag{A 8}$$

where $q_{vs,o} = (R_d/R_v)(e_{s,o}/p_o)$ is the saturation water vapour at the surface, with $\tilde{p}(z)/p_o$ and $f(z)$ given by (A 7). In our simulations, we will use $q_{vs,o} = 20\ \mathrm{g\ kg^{-1}}$ consistent with $e_{s,o} \approx 3500\ \mathrm{kg\ m^{-1}\ s^{-2}}$ and $p_o \approx 10^5\ \mathrm{kg\ m^{-1}\ s^{-2}}$ (see figure 3).

Appendix B. Derivation of total energy equation

The equation for total energy in (2.39) is derived from the FARE model (2.35)–(2.38) in the following way. First, taking the dot product of $\boldsymbol{u}$ with (2.35) yields

$$\frac{\mathrm{D}}{\mathrm{D}t}\left(\frac{\boldsymbol{u}\cdot\boldsymbol{u}}{2}\right) = -\boldsymbol{u}\cdot\nabla\phi + wb. \tag{B 1}$$

Next, the material derivative of the potential energy $\Pi(\theta_r, q_t, z)$ from (2.40) is

$$\frac{\mathrm{D}\Pi}{\mathrm{D}t} = \frac{\partial\Pi}{\partial\theta_r}\frac{\mathrm{D}\theta_r}{\mathrm{D}t} + \frac{\partial\Pi}{\partial q_t}\frac{\mathrm{D}q_t}{\mathrm{D}t} + \frac{\partial\Pi}{\partial z}\frac{\mathrm{D}z}{\mathrm{D}t} \tag{B 2}$$

$$= -\frac{\partial\Pi}{\partial\theta_r}\frac{L}{c_p}V_T\frac{\partial q_r}{\partial z} + \frac{\partial\Pi}{\partial q_t}V_T\frac{\partial q_r}{\partial z} - bw \tag{B 3}$$

$$= \left(\frac{\partial\Pi}{\partial q_t} - \frac{L}{c_p}\frac{\partial\Pi}{\partial\theta_r}\right)V_T\frac{\partial q_r}{\partial z} - bw. \tag{B 4}$$

For (B 4), the buoyancy and potential energy definitions in (2.28) and (2.40) are used to compute

$$\frac{\partial\Pi}{\partial q_t} = -g\left(\frac{L}{c_p\theta_o} - 1\right)(z - a) \quad \text{and} \quad \frac{L}{c_p}\frac{\partial\Pi}{\partial\theta_r} = -g\frac{L}{c_p\theta_o}(z - a) \quad \text{if } q_r > 0, \tag{B 5}$$

where it should again be noted that the definition of $\Pi(\theta_r, q_t, z)$ in (2.40) uses an integral with respect to z with θ_r and q_t held fixed.

Using (B 5) to continue with (B 4) leads to

$$\frac{\mathrm{D}\Pi}{\mathrm{D}t} = V_T g(z - a)\frac{\partial q_r}{\partial z} - bw \tag{B 6}$$

$$= \frac{\partial}{\partial z}[V_T g(z - a)q_r] - V_T g q_r - bw. \tag{B 7}$$

Combining (B 1) and (B 7) then leads to the final result (2.39). Note that the derivative calculations here are formal due to the possible discontinuity in derivatives of q_r (see its definition in (2.27)); the calculations should be understood as being taken from the corresponding integral formulation of the conservation law.

REFERENCES

ASAI, T. 1970 Stability of a plane parallel flow with variable vertical shear and unstable stratification. *J. Met. Soc. Japan* **48**, 129–139.

BANNON, P. R. 1996 On the anelastic approximation for a compressible atmosphere. *J. Atmos. Sci.* **53**, 3618–3628.

BARNES, G. M. & SIECKMAN, K. 1984 The environment of fast-and slow-moving tropical mesoscale convective cloud lines. *Mon. Weath. Rev.* **112** (9), 1782–1794.

BRETHERTON, C. S. 1987 A theory for nonprecipitating moist convection between two parallel plates. Part I: thermodynamics and 'linear' solutions. *J. Atmos. Sci.* **44**, 1809–1827.

CASTAING, B., GUNARATNE, G., KADANOFF, L., LIBCHABER, A. & HESLOT, F. 1989 Scaling of hard thermal turbulence in Rayleigh–Bénard convection. *J. Fluid Mech.* **204** (1), 1–30.

CHANDRASEKHAR, S. 1961 *Hydrodynamic and Hydromagnetic Stability*. Oxford University Press.

CUIJPERS, J. W. M. & DUYNKERKE, P. G. 1993 Large eddy simulation of trade wind cumulus clouds. *J. Atmos. Sci.* **50** (23), 3894–3908.

DEARDORFF, J. W. 1965 Gravitational instability between horizontal plates with shear. *Phys. Fluids* **8**, 1027.

DENG, Q., SMITH, L. M. & MAJDA, A. J. 2012 Tropical cyclogenesis and vertical shear in a moist Boussinesq model. *J. Fluid Mech.* **706**, 384–412.

EMANUEL, K. 1986 Some dynamical aspect of precipitating convection. *J. Atmos. Sci.* **43**, 2183–2198.

EMANUEL, K. A. 1994 *Atmospheric Convection*. Oxford University Press.

FOVELL, R. & OGURA, Y. 1988 Numerical simulation of a midlatitude squall line in two dimensions. *J. Atmos. Sci.* **45** (24), 3846–3879.

GRABOWSKI, W. W. & CLARK, T. L. 1993 Cloud–environment interface instability, part II: extension to three spatial dimensions. *J. Atmos. Sci.* **50**, 555–573.

GRABOWSKI, W. W. & MONCRIEFF, M. W. 2001 Large-scale organization of tropical convection in two-dimensional explicit numerical simulations. *Q. J. R. Meteorol. Soc.* **127**, 445–468.

GRABOWSKI, W. W. & SMOLARKIEWICZ, P. K. 1996 Two-time-level semi-Lagrangian modeling of precipitating clouds. *Mon. Weath. Rev.* **124** (3), 487–497.

GRABOWSKI, W. W., WU, X. & MONCRIEFF, M. W. 1996 Cloud-resolving modeling of tropical cloud systems during Phase III of GATE. Part I: two-dimensional experiments. *J. Atmos. Sci.* **53**, 3684–3709.

GRABOWSKI, W. W., WU, X., MONCRIEFF, M. W. & HALL, W. D. 1998 Cloud-resolving modeling of cloud systems during Phase III of GATE. Part II: effects of resolution and the third spatial dimension. *J. Atmos. Sci.* **55** (21), 3264–3282.

HENDON, H. H. & LIEBMANN, B. 1994 Organization of convection within the Madden–Julian oscillation. *J. Geophys. Res.* **99**, 8073–8084.

HOUZE, R. A. 1993 *Cloud Dynamics*. Academic.

HOUZE, R. A. Jr. 2004 Mesoscale convective systems. *Rev. Geophys.* **42**, G4003+.

JORGENSEN, D. P., LEMONE, M. A. & TRIER, S. B. 1997 Structure and evolution of the 22 February 1993 TOGA COARE squall line: aircraft observations of precipitation, circulation, and surface energy fluxes. *J. Atmos. Sci.* **54** (15), 1961–1985.

JUNG, J.-H. & ARAKAWA, A. 2005 Preliminary tests of multiscale modeling with a two-dimensional framework: sensitivity to coupling methods. *Mon. Weath. Rev.* **133** (3), 649–662.

KESSLER, E. 1969 *On the Distribution and Continuity of Water Substance in Atmospheric Circulations*, *Meteorological Monographs*, vol. 32. American Meteorological Society.

KHOUIDER, B., HAN, Y., MAJDA, A. J. & STECHMANN, S. N. 2012 Multiscale waves in an MJO background and convective momentum transport feedback. *J. Atmos. Sci.* **69**, 915–933.

KILADIS, G. N., WHEELER, M. C., HAERTEL, P. T., STRAUB, K. H. & ROUNDY, P. E. 2009 Convectively coupled equatorial waves. *Rev. Geophys.* **47**, RG2003.

KIM, D., SPERBER, K., STERN, W., WALISER, D., KANG, I.-S., MALONEY, E., WANG, W., WEICKMANN, K., BENEDICT, J., KHAIROUTDINOV, M., LEE, M.-I., NEALE, R., SUAREZ, M., THAYER-CALDER, K. & ZHANG, G. 2009 Application of MJO simulation diagnostics to climate models. *J. Climate* **22** (23), 6413–6436.

KLEIN, R. & MAJDA, A. 2006 Systematic multiscale models for deep convection on mesoscales. *Theor. Comput. Fluid Dyn.* **20**, 525–551.

KRISHNAMURTI, R. 1970*a* On the transition to turbulent convection. Part 1. The transition from two-to three-dimensional flow. *J. Fluid Mech.* **42** (2), 295–307.

KRISHNAMURTI, R. 1970*b* On the transition to turbulent convection. Part 2. The transition to time-dependent flow. *J. Fluid Mech.* **42** (2), 309–320.

KUO, H. L. 1961 Convection in conditionally unstable atmosphere. *Tellus* **13** (4), 441–459.

LAFORE, J. P. & MONCRIEFF, M. W. 1989 A numerical investigation of the organization and interaction of the convective and stratiform regions of tropical squall lines. *J. Atmos. Sci.* **46** (4), 521–544.

LAU, W. K. M. & WALISER, D. E. (Eds) 2011 *Intraseasonal Variability in the Atmosphere–Ocean Climate System*. Springer.

LEMONE, M. A., ZIPSER, E. J. & TRIER, S. B. 1998 The role of environmental shear and thermodynamic conditions in determining the structure and evolution of mesoscale convective systems during TOGA COARE. *J. Atmos. Sci.* **55** (23), 3493–3518.

LILLY, D. K. 1979 The dynamical structure and evolution of thunderstorms and squall lines. *Annu. Rev. Earth Planet. Sci.* **7**, 117–161.

LIPPS, F. B. & HEMLER, R. S. 1982 A scale analysis of deep moist convection and some related numerical calculations. *J. Atmos. Sci.* **39**, 2192–2210.

LIU, C. & MONCRIEFF, M. W. 2001 Cumulus ensembles in shear: implications for parameterization. *J. Atmos. Sci.* **58** (18), 2832–2842.

LUCAS, C., ZIPSER, E. J. & FERRIER, B. S. 2000 Sensitivity of tropical west pacific oceanic squall lines to tropospheric wind and moisture profiles. *J. Atmos. Sci.* **57** (15), 2351–2373.

MAJDA, A. & SOUGANIDIS, P. 2000 The effect of turbulence on mixing in prototype reaction–diffusion systems. *Commun. Pure Appl. Maths* **53** (10), 1284–1304.

MAJDA, A. J. & STECHMANN, S. N. 2008 Stochastic models for convective momentum transport. *Proc. Natl Acad. Sci. U.S.A.* **105**, 17614–17619.

MAJDA, A. J. & STECHMANN, S. N. 2009 A simple dynamical model with features of convective momentum transport. *J. Atmos. Sci.* **66**, 373–392.

MAJDA, A. J. & STECHMANN, S. N. 2011 Multiscale theories for the MJO. In *Intraseasonal Variability in the Atmosphere–Ocean Climate System* (ed. W. K. M. Lau & D. E. Waliser). Springer.

MAJDA, A. J. & XING, Y. 2010 New multi-scale models on mesoscales and squall lines. *Commun. Math. Sci.* **8** (1), 113–144.

MAJDA, A. J., XING, Y. & MOHAMMADIAN, M. 2010 Moist multi-scale models for the hurricane embryo. *J. Fluid Mech.* **657**, 478–501.

MAPES, B. E., TULICH, S., LIN, J.-L. & ZUIDEMA, P. 2006 The mesoscale convection life cycle: building block or prototype for large-scale tropical waves?. *Dyn. Atmos. Oceans* **42**, 3–29.

MONCRIEFF, M. W. 1981 A theory of organized steady convection and its transport properties. *Q. J. R. Meteorol. Soc.* **107** (451), 29–50.

MONCRIEFF, M. W. 1992 Organized convective systems: archetypal dynamical models, mass and momentum flux theory, and parameterization. *Q. J. R. Meteorol. Soc.* **118** (507), 819–850.

MONCRIEFF, M. W. 2010 The multiscale organization of moist convection and the intersection of weather and climate. In *Climate Dynamics: Why Does Climate Vary?* (ed. D.-Z. Sun & F. Bryan). *Geophysical Monograph Series*, vol. 189. pp. 3–26. American Geophysical Union.

MONCRIEFF, M. W. & GREEN, J. S. A. 1972 The propagation and transfer properties of steady convective overturning in shear. *Q. J. R. Meteorol. Soc.* **98** (416), 336–352.

MONCRIEFF, M. W. & MILLER, M. J. 1976 The dynamics and simulation of tropical cumulonimbus and squall lines. *Q. J. R. Meteorol. Soc.* **102**, 373–394.

MONCRIEFF, M. W., SHAPIRO, M., SLINGO, J. & MOLTENI, F. 2007 Collaborative research at the intersection of weather and climate. *WMO Bull.* **56**, 204–211.

MORRISON, H. & GRABOWSKI, W. W. 2008 Modeling supersaturation and subgrid-scale mixing with two-moment bulk warm microphysics. *J. Atmos. Sci.* **65** (3), 792–812.

NAKAZAWA, T. 1988 Tropical super clusters within intraseasonal variations over the Western Pacific. *J. Met. Soc. Japan* **66** (6), 823–839.

OGURA, Y. & PHILLIPS, N. A. 1962 Scale analysis of deep and shallow convection in the atmosphere. *J. Atmos. Sci.* **19**, 173–179.

PAULUIS, O. 2008 Thermodynamic consistency of the anelastic approximation for a moist atmosphere. *J. Atmos. Sci.* **65** (8), 2719–2729.

PAULUIS, O., BALAJI, V. & HELD, I. M. 2000 Frictional dissipation in a precipitating atmosphere. *J. Atmos. Sci.* **57** (7), 989–994.

PAULUIS, O. & DIAS, J. 2012 Satellite estimates of precipitation-induced dissipation in the atmosphere. *Science* **335** (6071), 953–956.

PAULUIS, O. & SCHUMACHER, J. 2010 Idealized moist Rayleigh–Bénard convection with piecewise linear equation of state. *Commun. Math. Sci.* **8**, 295–319.

PAULUIS, O. & SCHUMACHER, J. 2011 Self-aggregation of clouds in conditionally unstable moist convection. *Proc. Natl Acad. Sci. U.S.A.* **108**, 12623–12628.

PETERS, N. 2000 *Turbulent Combustion*. Cambridge University Press.

PRUPPACHER, H. R. & KLETT, J. D. 1997 *Microphysics of Clouds and Precipitation*. Kluwer Academic.

ROGERS, R. R. & YAU, M. K. 1989 *A Short Course in Cloud Physics*. Butterworth–Heinemann.

SCHUMACHER, J. & PAULUIS, O. 2010 Buoyancy statistics in moist turbulent Rayleigh–Bénard convection. *J. Fluid Mech.* **648**, 509–519.

SEITTER, K. L. & KUO, H.-L. 1983 The dynamical structure of squall-line type thunderstorms. *J. Atmos. Sci.* **40**, 2831–2854.

SPIEGEL, E. A. & VERONIS, G. 1960 On the Boussinesq approximation for a compressible fluid. *Astrophys. J.* **131**, 442–447.

SPYKSMA, K. & BARTELLO, P. 2008 Small-scale moist turbulence in numerically generated convective clouds. *J. Atmos. Sci.* **65**, 1967–1978.

SPYKSMA, K., BARTELLO, P. & YAU, M. K. 2006 A Boussinesq moist turbulence model. *J. Turbul.* **7**, 1–24.

STEVENS, B. 2005 Atmospheric moist convection. *Annu. Rev. Earth Planet. Sci.* **33** (1), 605–643.

STEVENS, B. 2007 On the growth of layers of nonprecipitating cumulus convection. *J. Atmos. Sci.* **64**, 2916–2931.

STRAUB, K. H., HAERTEL, P. T. & KILADIS, G. N. 2010 An analysis of convectively coupled Kelvin waves in 20 WCRP CMIP3 global coupled climate models. *J. Climate* **23** (11), 3031–3056.

SUKHATME, J., MAJDA, A. J. & SMITH, L. M. 2012 Two-dimensional moist stratified turbulence and the emergence of vertically sheared horizontal flows. *Phys. Fluids* **24**, 036602.

VALLIS, G. K. 2006 *Atmospheric and Oceanic Fluid Dynamics: Fundamentals and Large-scale Circulation*. Cambridge University Press.

WU, X., GRABOWSKI, W. W. & MONCRIEFF, M. W. 1998 Long-term behavior of cloud systems in TOGA COARE and their interactions with radiative and surface processes. Part I: two-dimensional modeling study. *J. Atmos. Sci.* **55** (17), 2693–2714.

WU, X. & MONCRIEFF, M. W. 1996 Collective effects of organized convection and their approximation in general circulation models. *J. Atmos. Sci.* **53** (10), 1477–1495.

XU, K. M. & RANDALL, D. A. 1996 Explicit simulation of cumulus ensembles with the GATE Phase III data: comparison with observations. *J. Atmos. Sci.* **53**, 3710–3736.

ZHANG, C. 2005 Madden–Julian oscillation. *Rev. Geophys.* **43**, G2003+.